EXPERIMENTAL DYNAMIC FORCED PERFORMANCE OF A CENTRALLY GROOVED, END SEALED SQUEEZE FILM DAMPER

A Thesis

by

LADY PAOLA MAHECHA MOJICA

Submitted to the Office of Graduate Studies of
Texas A&M University
in partial fulfillment of the requirements for the degree of

MASTER OF SCIENCE

August 2011

Major Subject: Mechanical Engineering

EXPERIMENTAL DYNAMIC FORCED PERFORMANCE OF A CENTRALLY GROOVED, END SEALED SQUEEZE FILM DAMPER

A Thesis

by

LADY PAOLA MAHECHA MOJICA

Submitted to the Office of Graduate Studies of
Texas A&M University
in partial fulfillment of the requirements for the degree of

MASTER OF SCIENCE

Approved by:

Chair of Committee,	Luis San Andrés
Committee Members,	Alan Palazzolo
	Giovanna Biscontin
Head of Department,	Dennis O'Neal

August 2011

Major Subject: Mechanical Engineering

ABSTRACT

Experimental Dynamic Forced Performance of a Centrally Grooved, End Sealed Squeeze Film Damper. (August 2011)

Lady Paola Mahecha Mojica, B.En.; B.En., Universidad de los Andes at Bogotá, Colombia

Chair of Advisory Committee: Dr. Luis San Andrés

Squeeze film dampers (SFDs) provide viscous damping to attenuate excessive vibrations and enhance system stability in turbomachinery. SFDs are of special importance in aircraft engines which use rolling element support bearings that, by themselves, do not provide enough damping to ensure safe operation.

A modular test rig capable of simulating actual operating conditions in aircraft jet engines is used to test two centrally grooved, end sealed, SFDs. Both SFDs have diameter D and nominal radial clearance c and consist of two parallel squeeze film lands separated by a deep circumferential groove of length L_G and depth d_G. A short length damper with film land lengths L and a long damper with land lengths $2L$ are tested.

Piston rings seal the damper lands. An ISO VG2 lubricant is supplied to the SFD via three radial holes that discharge lubricant into the central groove. The lubricant passes through the damper lands and across the piston ring seals to finally exit the damper at ambient pressure.

Circular orbit tests of amplitude ~0.5c and for static eccentricities varying from 0 to ~0.36c are conducted on the two sealed dampers. The instrumental variable filter method (IVFM) serves to identify the SFD dynamic force coefficients. The parameter identification range is 50Hz to 210Hz for the short damper and 110Hz to 250Hz for the long damper.

Large amplitude dynamic pressures measured in the central groove demonstrate that the central groove does not divide the damper in two separate film lands, but the lubricant in the groove interacts with the squeeze film lands, hence contributing significantly to the SFD forced response. Dynamic pressures in the film lands and in the central groove reveal that both dampers operate free of air ingestion or cavitation for the tested static eccentricities and amplitudes of motion.

Comparisons to test results for the same SFD configurations but with open ends demonstrate the effectiveness of the end seals on increasing the direct damping coefficients. For the sealed ends short length damper, the added mass coefficients are ~2 times larger and the damping coefficients are ~3.8 times larger than the respective coefficients of the open ends long damper. For the sealed ends long damper, the damping coefficients are ~2.8 times, and the added mass coefficients are ~3.1 times larger than coefficients from the open ends configuration.

The identified SFD direct stiffness coefficients are nearly zero except at the maximum static eccentricity for the long damper.

Predictions from a novel computational model that include the effects of the central groove, the lubricant feed holes and the end seals are in excellent agreement with results from the short length damper. For the long damper, the predicted damping coefficients are in good agreement with the test results, while the added mass coefficients are under predicted by ~25%.

Experimental results from the two sealed SFD configurations lead to a better understanding of the effects of end seals as well as central feed groves on the SFD forced performance. The results presented in this thesis will help improve the effectiveness of SFDs aircraft jet engines.

DEDICATION

To my family

ACKNOWLEDGEMENTS

I would like to thank Dr. Luis San Andrés, my advisor and committee chair, for his guidance, support and for allowing me the opportunity to be a part of the Tribology Group throughout my time at Texas A&M.

Thanks to fellow students, Sanjeev Seshagiri, Alain Anderson, Michael Vannarsdall Sarabeth Froneberger, James Law, Logan Havel, Brian Butler, and Thomas Chiratadam,

At the Turbomachinery Laboratory, I thank Eddie Denk and Ray Mathews.

Finally, I gratefully acknowledge the contributions of the technical contract monitors, Dr. Reng Lin and Dr. John Wang, from Pratt & Whitney Engines.

NOMENCLATURE

$a_{X(t)}$, $a_{Y(t)}$	Absolute BC acceleration components along X and Y directions [m/s^2]
c	Squeeze film land nominal radial clearance [m]
c_A,c_B	Measured radial clearances of film lands with journals A and B [m]
$C_{\alpha\beta,\ (\alpha,\beta= X,Y)}$	SFD damping coefficients [N.s/m]
C^*	Predicted direct damping coefficients from classical lubrication analysis [Ns/m] , Eq.(D1)
C_T, C_B	Hydraulic conductances of the top and bottom damper lands [LPM/bar]
C_{TS}, C_{BS}	Hydraulic conductances of the top and bottom end seals [LPM/bar]
$(\bar{C}_{XX}, \bar{C}_{YY})_{SFD}$	Normalized (dimensionless) SFD direct damping coefficients (=C/C^*)
$(C_s)_{\alpha\beta,(\alpha,\beta= X,Y)}$	Identified remnant damping coefficients of the dry structure [Ns/m]
d_G	Physical (actual) groove depth [m]
d_η	Effective groove depth [m]
D	Journal diameter [m]
e_S	BC static eccentricity along 45^o [m]
e_X, e_Y	BC eccentricity components along X and Y axes [m]
f_n	Natural frequency of the test system, dry or lubricated [Hz] (=$\omega_n/2\pi$)
f_{start}, f_{end}	Start and end frequencies for test system parameter identification [Hz]
$F_{X(t)}$, $F_{Y(t)}$	Applied shaker loads along X and Y directions [N]
$G_{\alpha\beta}$, $(\alpha,\beta=X,Y)$	Flexibility functions [m/N]
h	Lubricant film thickness [m]
$H_{(\omega)}$	Impedance function [N/m]
K_S	Static stiffness [N/m]
$(K_s)_{\alpha\beta,(\alpha,\beta= X,Y)}$	Identified test rig structural stiffness [N/m]
L,L_G	Land length and groove length [m]
L_A, L_B	Film land lengths for the long and short length damper [m]

$M_{\alpha\beta,\ (\alpha,\beta= X,Y)}$	SFD added mass coefficients [kg]
M^*	Predicted direct added mass coefficients from classical lubrication analysis [kg], Eq. (D1)
M_{BC}	Mass of BC [kg]
$(\bar{M}_{XX}, \bar{M}_{YY})_{SFD}$	Normalized (dimensionless) SFD direct damping coefficients (=M/M^*)
$(M_s)_{\alpha\beta,(\alpha,\beta= X,Y)}$	Identified residual masses of dry structure [kg]
P	Dynamic pressure in film land [bar]
P_a, P_{cav}	Ambient pressure and lubricant cavitation pressure [bar]
P_{in}, P_G	Lubricant pressures at journal inlet and in the central groove [bar]
Q_{in}, Q_{out} , Q_T, Q_B	Lubricant flow rates: Inlet, outlet, top damper, bottom damper [LPM]
r	Amplitude of circular motion [m]
R	Journal radius [m] (=$D/2$)
Re_{s*}	Squeeze film Reynolds number, ($=\rho\omega c^2/\mu$)
R_T, R_B	Hydraulic resistances of the top and bottom damper film lands [LPM/bar]
R_{TS}, R_{BS}	Hydraulic resistances of the top and bottom end seals [LPM/bar]
t	Time [s]
T	Lubricant temperature [^{o}C]
τ	Dimensionless time [=$t2\pi/\omega$]
U_C, U_K, U_M	Uncertainties in damping [Ns/m], stiffness [N/m] and inertia [kg] coefficients
U_δ, U_ω	Uncertainties in measurement of displacement [m] and frequency [Hz]
V	Known volume of the oil collector tray [liters]
$x_{(t)}$, $y_{(t)}$	BC displacements relative to the journal along X and Y directions [m]
δ	General notation for BC displacements (used in uncertainty analysis) [m]
ξ, ξ_s	Damping ratios of the lubricated and dry systems
θ	Angular coordinate to specify angular locations on the BC [degrees]
ρ	Lubricant density [kg/m^3]
μ	Lubricant viscosity [Pa.s]

ω, ω_n	Excitation frequency, natural frequency [rad/s]

Matrices and Vectors

$\mathbf{a}$	$\{ a_{X(t)}, a_{Y(t)}\}^T$, Vector of BC accelerations in the time domain [m/s^2]
$\bar{\mathbf{a}}$	Discrete Fourier Transform (DFT) of time domain BC accelerations [m/s^2]
$\mathbf{A}$	Matrix of stacked real and imaginary parts of flexibility functions at each frequency ω [N/m]
$\mathbf{C_S}$, $\mathbf{C}$, $\mathbf{C_{SFD}}$	Matrices of damping coefficients of dry structure, lubricated system and squeeze film [Ns/m]
$\mathbf{F}_{(t)}$	$\{F_{X(t)}, F_{Y(t)}\}^T$, Vector of applied forces in time domain on support structure [N]
$\bar{\mathbf{F}}_{(\omega)}$	Discrete Fourier Transform (DFT) of applied force vectors [N]
$\bar{\mathbf{F}}_{M(\omega)}$	Reduced force vector ($\bar{\mathbf{F}}_{(\omega)}$ - $M_{BC}\,\bar{\mathbf{a}}$) [N]
$\mathbf{G}$, $\mathbf{G_{dry}}$	Flexibility functions of the lubricated and dry systems [m/N]
$\mathbf{H}$, $\mathbf{H_{dry}}$	Impedance functions of the lubricated and dry systems [N/m]
$\mathbf{I}$	Identity matrix
$\mathbf{K_s}$, $\mathbf{K}$, $\mathbf{K_{SFD}}$	Matrices of stiffness coefficients of dry structure, lubricated system and squeeze film [N/m]
$\mathbf{M_s}$, $\mathbf{M}$, $\mathbf{M_{SFD}}$	Matrices of inertia coefficients of dry structure, lubricated system and squeeze film [kg]
$\mathbf{z}$	$\{x_{(t)}, y_{(t)}\}^T$, Vector of BC displacements in the time domain [m]
$\bar{\mathbf{z}}_{(\omega)}$	Discrete Fourier Transform (DFT) of time domain BC displacements [N]

Subscripts

k	Frequency index for single frequency excitation
A,B	Long and short journals

TABLE OF CONTENTS

CHAPTER Page

Page

LIST OF TABLES

Page

Page

LIST OF FIGURES

Page

Page

Page

Page

CHAPTER I

INTRODUCTION

A squeeze film damper (SFD) is a mechanical device that provides damping in rotating machinery to attenuate rotor vibrations and to enhance system stability. SFDs are most commonly used in aircraft jet engines to provide damping to rolling element support bearings.

Figure 1 shows a typical SFD configuration consisting of a stationary outer bearing and an inner journal mechanically prevented from spinning but free to whirl. A lubricant fills the annular clearance between the journal and the bearing to form the squeeze film.

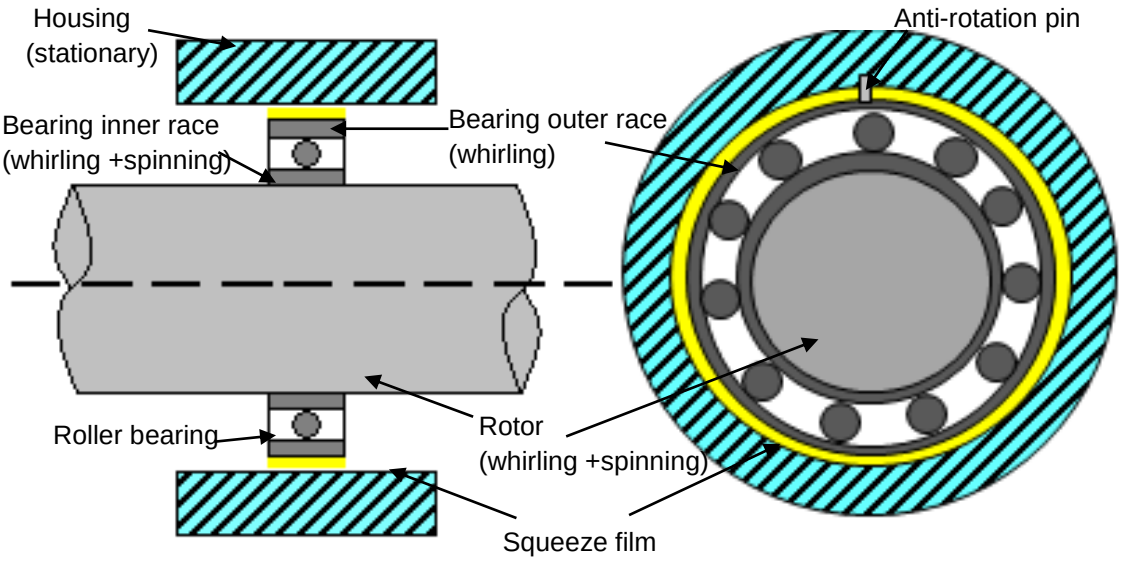

Figure 1. Schematic drawing of a rotor supported on ball bearings and a squeeze film damper (SFD)

This thesis follows the style of Journal of Tribology.

SFD geometry (clearance, length, diameter) and operating conditions (centering, amplitude of motion, supply pressure etc.) determine the SFD dynamic forced performance [1]. Some SFDs implement feed and discharge grooves to ensure even lubricant flow into the damper film lands. In several investigations [2-7], the dynamic pressure in the groove is found to be as large as the pressure in the squeeze film land, demonstrating that grooves greatly affect the SFD forced performance.

Under certain operating conditions, air is ingested into the squeeze film lands. Air ingestion severely reduces the damping capability and is more pervasive for an open ends configuration, with lubricant supplied at low pressures, under high excitation frequency, and under large amplitudes of journal whirl motion [8]. This undesired operating condition can be ameliorated with the use of end seals[9], which aid to increase the damping capability and also require of a lesser lubricant flow [1]. Commonly used seals include piston ring seals, O-rings and end plates [10].

I.1 Justification

New aircraft engine designs push limits on their size, weight, operating speeds and rotor flexibility, thus resulting in large rotor vibrations and calling for the exploration of new SFD geometries with proven forced performance [11].

SFDs have been studied for over five decades; however, there are aspects of damper operation and film geometry that affect their forced performance and have not been either accurately modeled or experimentally verified [12].

Due to the large number of possible SFD configurations and operating regimes, there is a need to experimentally determine the behavior of SFDs under various operating conditions and to obtain a better understanding of SFD forced performance. Since in most practical applications a SFD will not operate at its centered position [13]. Of particular interest is to quantify the forced performance of SFDs when operating at increasing static journal eccentricities. Some experimental and theoretical works have

addressed SFDs operating at static eccentric positions [13, 14]; however, predicted results generally do not support experimental data.

The current work aims to generate benchmark SFD empirical data for two sealed squeeze film dampers that incorporate a deep circumferential central feed groove and to compare the data with predictions from a finite element computational analysis (PW_SFD_2010©) [15]. The experimental force coefficients are obtained from circular orbits in a dedicated test rig for operation at centered and off-centered static eccentricities.

I.2 Objective

The objective of the current effort is to experimentally study the dynamic forced response of a centrally grooved and end sealed squeeze film damper, operating at increasing static eccentric positions, to generate benchmark SFD experimental data. A test rig which permits the exchange of damper journal as well as the support stiffness is used to test two SFDs. Two journals, A and B, render a SFD with two parallel squeeze film lands separated by a deep circumferential groove of length L_G=12.7 mm and depth d_G=9.525 mm. Journal A makes axial film land lengths L_A=25.4 mm and is twice as long as journal B (L_B=12.7 mm). Both damper configurations have a nominal radial clearance c=127 μm.

CHAPTER II

LITERATURE REVIEW

Della Pietra and Adiletta [12, 16] present an extensive review of past research in squeeze film dampers covering Cooper's first SFDs investigation in 1963 [17] through 2002. This review comprises theoretical and experimental research efforts on SFDs, including the study of circumferential feeding grooves and sealed ends configurations affecting SFD forced performance.

Experimental research on dampers with central feeding grooves [2, 3, 18] reveal dynamic pressures in the feeding groove to be as large as those in the squeeze film lands, thus demonstrating a clear flow interaction between the groove and the film lands. This behavior contradicts classical lubrication theory predictions in which the central groove effectively separates the SFD into two damper film lands. Before 1992, the discrepancies between experimental results with classical lubrication theory predictions were attributed to the flow interaction between fluid in the squeeze film lands and the fluid in the central feed groove; however, no attempts to model the effects of the groove in the SFD forced response were pursued.

San Andrés [4] develops a model that incorporates the volume-fluid compressibility effect in a central feed groove on the forced response of a short length damper. The analysis is valid for small amplitudes of journal motion at a centered position. The model accounts for a dynamic fluid interaction between the feeding groove and the squeeze film lands. The model predictions of direct damping and added mass coefficients agree with experimental results reported by Ramli *et al.* [3]. Both the model and the experimental results prove that for low excitation frequencies a centrally grooved SFD behaves as a damper with a single film land.

To validate the model given in Ref. [4], Arauz and San Andrés [5] obtain benchmark data from experiments on a short length SFD with a single land, for an open and a partially sealed ends configurations. In these experiments, fluid inertia effects are found

to be negligible in both configurations. Then, in Ref. [6] the same authors present a theoretical and experimental study with circumferentially grooved SFDs of increasing groove depths and journal orbital motion an open ends short length damper. Experimentally derived tangential forces at the groove are relatively large, which contribute considerably to the SFD damping capability. The experimental radial forces in the groove and in the film lands are significant. Thus experiments demonstrate that the groove induces fluid inertia effects in the damper film lands. In Ref. [6] the original model developed by San Andrés [4] is extended to include circumferential flow in the central groove.

Qingchang *et al.* [19] present an analytical study of grooved SFDs. The central feed groove is modeled as a "*special damper*". In the model the variations of fluid pressure and velocity in the feed groove are included in the Navier Stokes equations. The results presented in this paper are misleading by ascertaining that a circumferential groove does not affect the SFD radial forces, i.e., the circumferential groove does not induce fluid inertia effects. Archival literature, including experimental and theoretical work on SFDs with circumferential grooves [4, 6, 7, 20-23], proves that a feed groove indeed generates fluid inertia effects.

Levesley *et al.* [24] conduct experiments to assess the effects of oil feed holes, sealing arrangements and circumferential feeding groove location on the damping capacity of different SFDs configurations. The piston-rings sealed SFD gives the most damping compared to that in either end-chambered or end-plate seal SFD arrangements.

Air entrainment is a detriment to the damping ability of SFDs. Air entrainment occurs most commonly in open ends configurations while operating with low oil feed pressures and with journals performing large amplitudes of motion at high whirl frequencies. Diaz and San Andrés [25, 26] carry out tests on a squeeze film damper supplied with a controlled air-lubricant mixture ranging from 0% to 100% air content. The damping coefficient decreases as the air content increases. In Ref. [27], Diaz and San Andrés develop a model based on a modified Reynolds equation to predict the forced performance of SFDs operating with a homogeneous air-in-oil mixture. An

empirical formula to estimate the amount of air entrained in the squeeze film lands in terms of the damper geometry (length, diameter), and operating conditions (excitation frequency, orbit radius, flow rate) is advanced. Experimental data in Ref. [25, 26] correlate well with the model prediction.

SFDs usually implement end seals to increase the damping capacity, while reducing the through flow. End seals also aid to reduce air entrainment[9]. To date, only experiments can determine the best sealing type configurations[1]. Extensive literature reports the study of sealed SFD configurations [20-23]. The next section summarizes literature concerning the effects of sealed ends on the forced performance of SFDs.

Lund *et al*. [22] theoretically and experimentally investigate the effects of a circumferential groove in a sealed SFD. The theoretical model, using a perturbation method, proposes that the acceleration terms are inversely proportional to the groove depth. Both experimental and predicted added mass coefficients increase with groove depth; however, experimental results are well predicted only at low groove depths. As the groove depths increases, the discrepancy between experimental and predicted SFD force coefficients increases, thus demonstrating data that is contrary to the model premise. The influence of end seals on SFD forced performance is not investigated.

Kim and Lee [23] theoretically and experimentally study a short length sealed SFD with a circumferential feeding groove. They present an analysis of the recorded dynamic pressure fields due to dynamic loads generated by an active magnetic bearing that accounts for the effects of the end seals and the circumferential groove. The model is valid for dampers with small groove width (L_G) to film land length (L) ratios ($L_G/L<<1$) and operation at a centered condition. The fluid in the groove is taken as compressible, its compressibility factor being frequency dependent. A series of experiments with single and two stage liquid seals and for different seal gaps is conducted. The model predictions correlate well with experimentally identified force coefficients.

San Andrés and Delgado [28, 29] test a SFD with a contact mechanical end seal. The force coefficients are determined from unidirectional and circular centered orbits (CCOs) tests. The seal dry-friction coefficient, originated from the surfaces in contact, is

modeled as an equivalent viscous damping coefficient, which decreases with excitation frequency and orbit radius. Experimentally identified SFD damping force coefficients are independent of the excitation frequency and increase with the amplitude of journal motion. The damping coefficients are determined from a two-step procedure, which requires, first, testing with the damper free of lubricant and, then, testing when it is lubricated. Significant dynamic pressures in the discharge groove corroborate the considerable influence of grooves in the damper forced performance. The mechanical seal is shown to effectively prevent air ingestion into the damper film land. Identified SFD force coefficients agree well with predictions based on the full film, short length damper model modified with fluid inertia effects. In Ref. [30], the authors advance a nonlinear identification parameter which requires lubricated tests with three different amplitudes of journal motion to determine the mechanical seal coefficients and the SFD coefficients simultaneously.

Delgado *et al.* [31, 32] present a linear fluid inertia bulk-flow model to predict the dynamic forced performance of grooved SFDs and oil seals. In the model, the groove is divided in two regions, a thru flow and a recirculation region, so only a fraction of the groove depth (denominated effective groove depth) is active. The theoretical analysis shows large radial forces in the grooves producing large added mass coefficients. Predictions of the damping and added mass coefficients are in excellent agreement with experimental results in Ref. [28, 29]. However, only experimental work or CFD simulations can determine the actual effective groove depth to be used in the predictive model.

Arghir *et al*.[33] present a theoretical analysis of SFD forced performance using bulk flow equations. This novel model includes the effects of feeding orifices, circumferential groove, and end seal piston ring opening on the dynamic forced response of a SFD. Predicted tangential and radial forces are in good agreement with experimental data in Ref. [34]. Since the bulk flow model includes fluid inertia effects, the model predictions are in better agreement with experimental data than when compared to results from a Reynolds equation based numerical approach.

This review discusses past work on SFDs relevant to the objectives of this thesis. Despite the large amount of research on SFDs; several SFD geometries, seal configurations and operating conditions have not been researched. Thus, more experimental and theoretical work is required to better understand SFDs performance. The current work attempts to expand the knowledge on the influence of end seals and central feed groove on SFD forced performance.

CHAPTER III

TEST RIG DESCRIPTION

Figure 2 shows the main components of the test rig assembly, consisting of a journal and a bearing assembly supported on a massive pedestal, which is rigidly fastened to a steel table. Figure 3 depicts the bearing assembly formed by a bearing cartridge (BC) supported on a number of support roods. The support structure consists of a 16 steel rod arrangement: four main support rods (separated 90^{o}) to hold and align the BC and 12 flexural rods that can be added or removed to change the support stiffness. The BC accommodates most of the instrumentation and attachments for ancillary systems that serve to dynamically and statically displace the BC. A deep circumferential groove is machined in the mid-plane of the BC.

A journal base and a damper journal form the journal assembly shown in Figure 4. The journal base is fixed to the pedestal and an oil collector is placed on the lower end of the base journal. The damper journal is rigidly attached to the base by a center bolt. This design allows for the journals (A and B) to be easily exchanged between tests without major changes in the instrumentation setup.

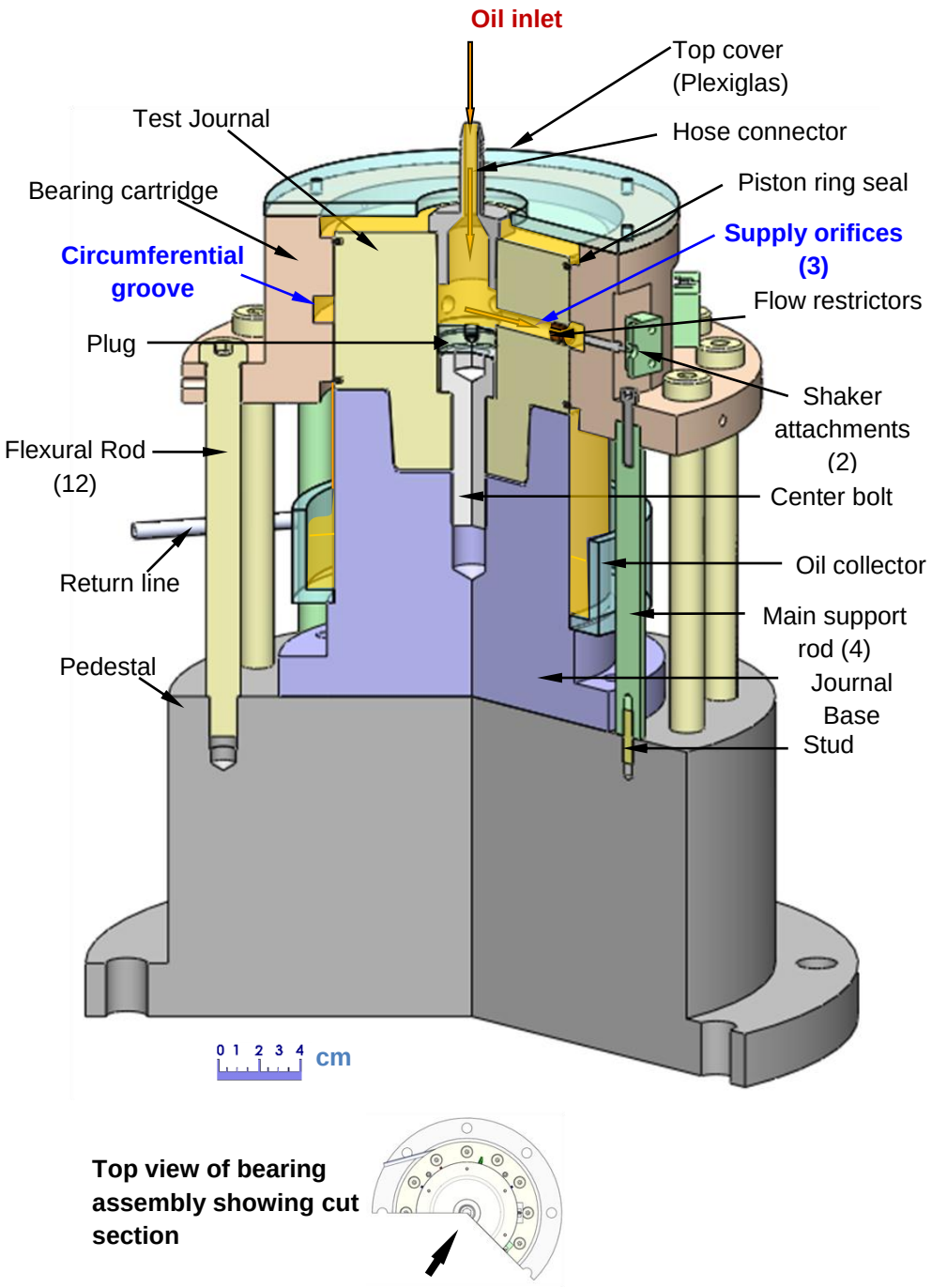

Figure 2. Cut section view of SFD assembly [35, 36]

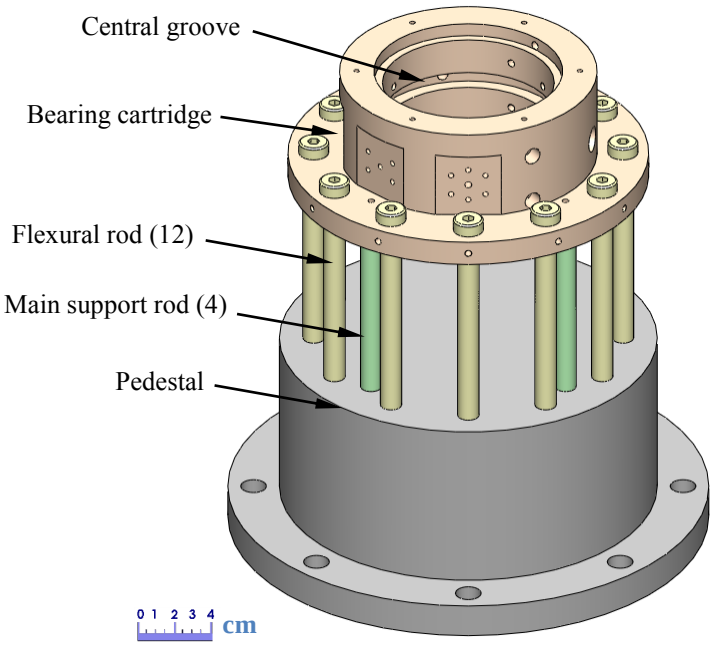

Figure 3. Isometric view of bearing assembly [36]

To feed oil into the damper lands, the journal has a central vertical hole that connects to three radial orifices (120^{o} apart) that exit to the central groove. Orifice restrictors (2.57 mm in diameter) at the end of the supply orifices regulate the lubricant flow into the central groove.

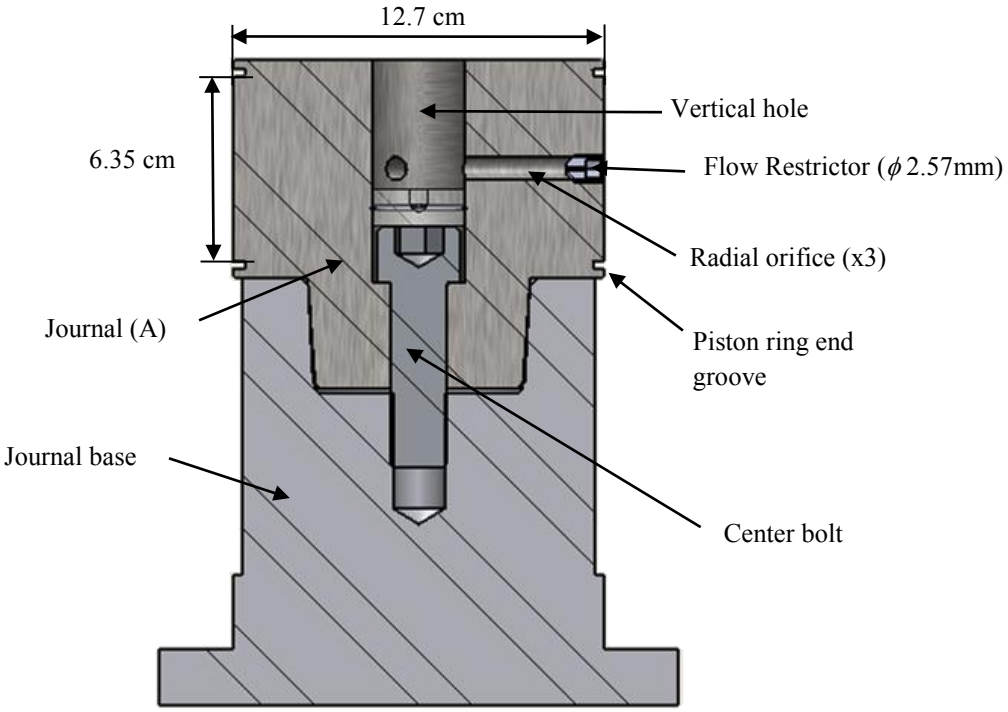

Figure 4. Cut view of journal assembly (journal A installed)

The gap between the journal outer face and the BC inner face forms the SFD. Figure 5 shows two different journals, A and B, that when installed in the journal base, render a SFD with two parallel squeeze film lands separated by a deep groove (L_G=12.7 mm, d_G=9.525 mm). The film lengths equal L_A=25.4 mm for journal A and L_B=12.7 mm for journal B. The measured (average) radial clearances are c_A=141μm and c_B= 138μm. The central circumferential groove, of width L_G=12.7 mm and depth d_G=9.525mm, supplies oil uniformly to the two squeeze film lands top and bottom. At the top land the oil leaves the damper through an oil return line and at the bottom the lubricant is received in the oil collector connected to a second return line.

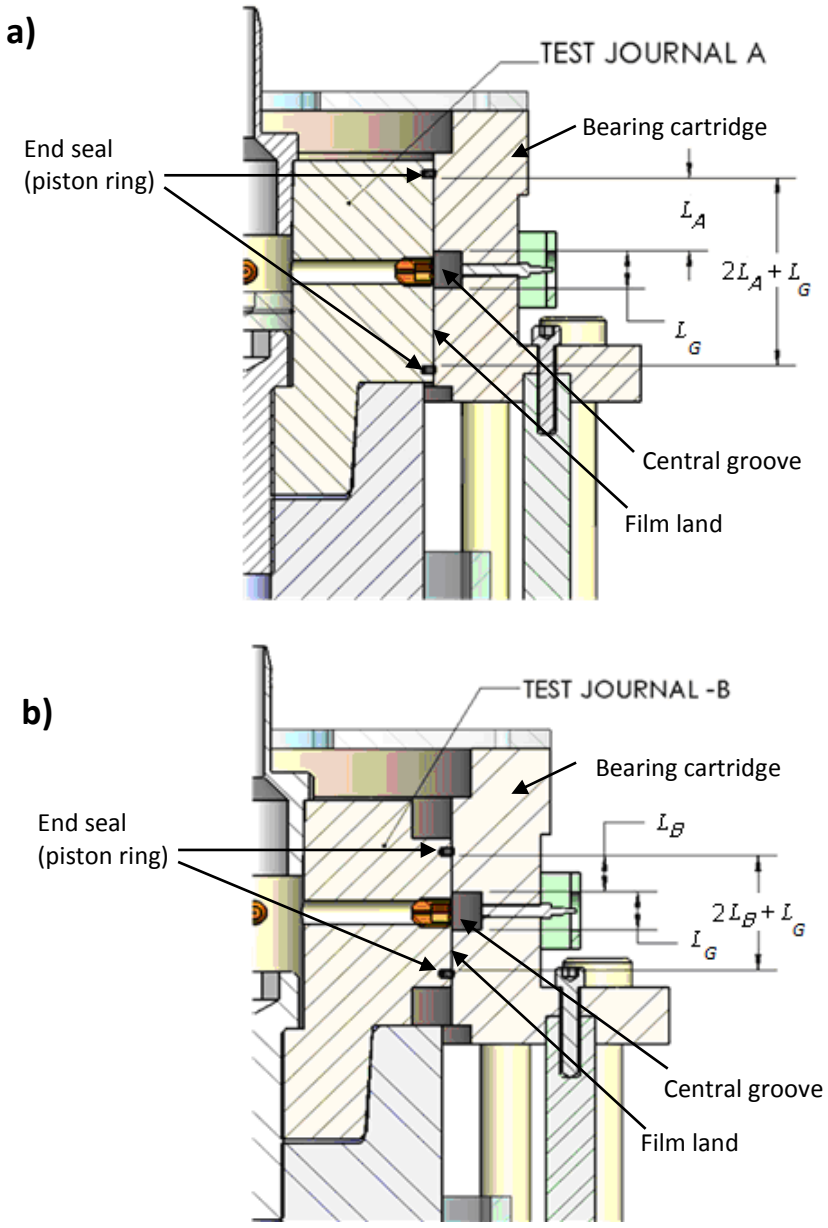

Figure 5. Cross section of bearing assembly (a) setup A- SFD land length L_A=2.54 cm, and (b) setup B- SFD land length L_B=1.27cm [36]

To increase the squeeze film damping while reducing the axial through flow, piston ring seals can be installed. A piston ring is an open-ended ring that fits into end grooves machined in the journal and seals the gap between the journal and the BC. Figure 6 shows piston ring installed in the long journal and details the piston ring opening (slits).

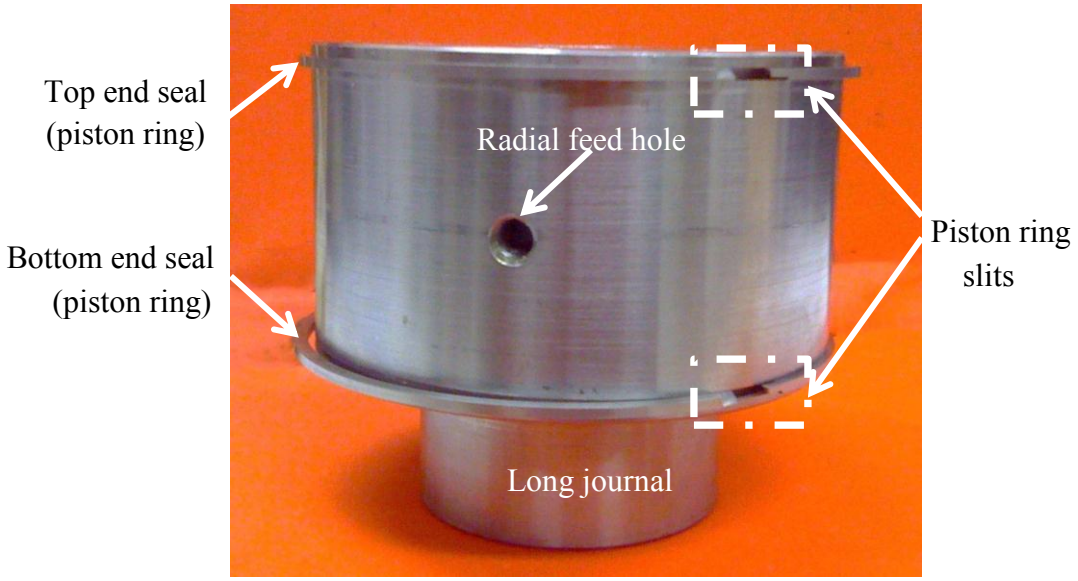

Figure 6. Piston rings installed in end grooves, machined in short length journal

This type of piston ring has a different flow conductance depending on the orientation it is installed. Figure 7 displays the two faces of the piston ring, denominated A and B, and their closing ends. The figure shows face A making a radial slit while face B makes a staggered slit. Faces A and B can either be installed towards ambient pressure or towards a film land [37].

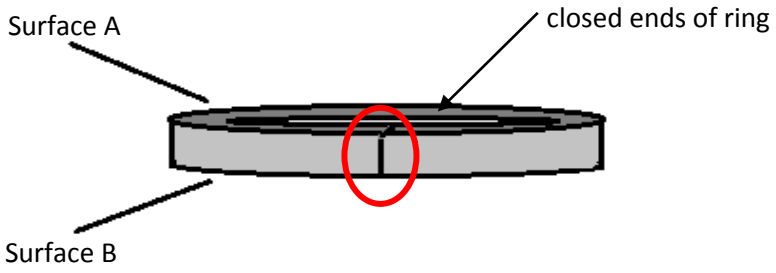

Figure 7. Schematic views of closed piston ring and its faces showing slits [37]

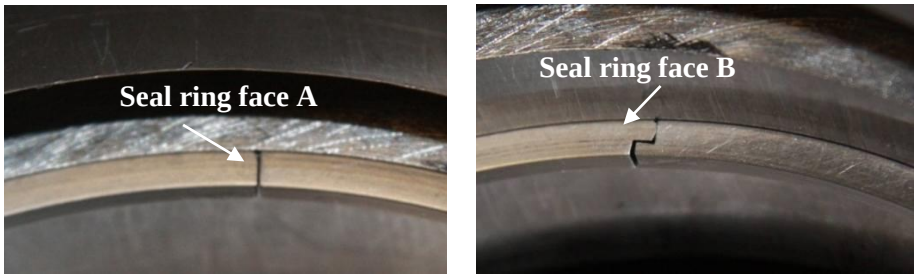

Figure 7. Continued

Ref. [37] details the four possible sealing arrangements; and demonstrates that a configuration with face B of the seals facing to ambient pressure provides the largest flow resistance. Dynamic load tests are conducted with this installation.

Figure 8 shows the piston ring installer, an external tool that has a tapered inner surface and fits on top of the bearing cartridge, used to compress the seal ring into the end grooves as the journal is lowered inside the BC. The circumferential groove has three rims separated 120^{o}, to compress the bottom ring and prevent it from expanding in the central groove during installation. Figure 9 displays a top view of the BC showing one of the rims in the groove.

Figure 8. Piston ring installer[36]

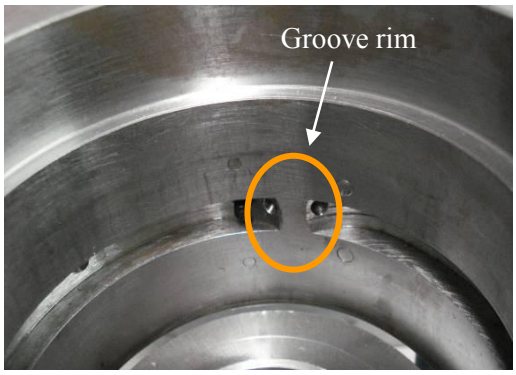

Figure 9. Central groove rim to prevent piston ring from expanding

Figure 10 shows a top view of the test rig assembly and the ancillary systems. Two electromagnetic shakers orthogonally positioned are attached to the BC through slender stingers. These shakers induce motion of the BC. A static loader mechanism positioned 45^{o} away from the shakers can displace the BC to various static eccentricities.

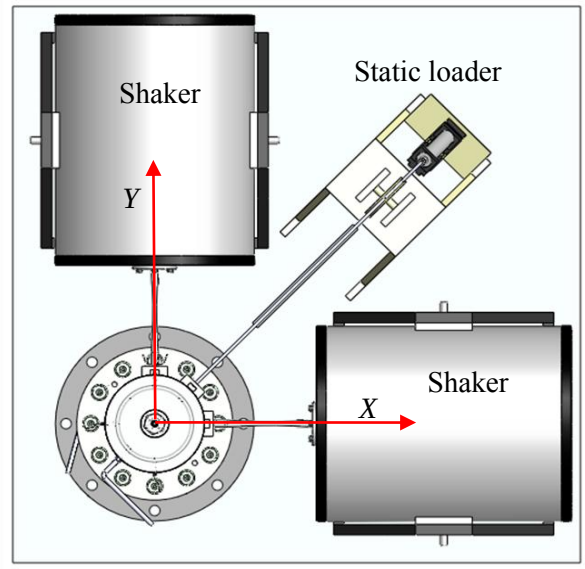

Figure 10. Top view of SFD test rig and ancillary systems [36]

III. 1 Instrumentation and data acquisition system

A DAQ system generates shaker control signals and acquires static and dynamic signals from numerous sensors positioned in the BC. Table 1 lists the sensor names, manufacturer, sensitivities, measurement range and use in the test rig. The static signals are inlet and outlet (top and bottom) temperatures; and static displacement of the BC. Dynamic signals include the applied loads ($F_{X(t)}$, $F_{Y(t)}$), the relative displacements between the BC and the journal ($X_{(t)}$, $Y_{(t)}$), the accelerations of the BC ($a_{X(t)}$, $a_{Y(t)}$); and dynamic pressure signals at the film lands and the central grove at various radial locations.

Table 1. List of sensors and other digital equipment in P&W SFD test rig [35]

Sensor	Manufacturer	Model	Sensitivity	Measurement variable
REBAM eddy current (2)	Bently-Nevada®	7200 series	39.37 V/mm (REBAM)	Bearing cartridge displacement with respect to journal along *X* and *Y* axes
Accelerometer (2)	PCB®	353B33	106 mV/g	Bearing accelerations along *X* and *Y* axes
Piezoelectric pressure sensor (6)	PCB®	111A26	72.5 mV/bar and 145 mV/bar	Dynamic pressure in groove (2), upper film land (2) and lower film land (2)
Piezoelectric load cell (2)	PCB®	208C03	2.24 mV/N	Dynamic load on bearing cartridge applied by shakers along *X* and *Y* directions
Strain-gage type pressure transducer (1)	Omega®	PX313-100G5V	0.725 mV/bar	Inlet pressure of lubricant in supply line before entering journal
Strain gage type load cell (1)	Omega®	LC213-500	8.99 mV/kN	Magnitude of static load applied on bearing cartridge to generate off-centered operation
Thermocouple (3)	Omega®	K type	0.072 mV/°C	Temperature of lubricant at journal inlet, exit of top and bottom lands
Flowmeter (1)	GPI ®	A1 Series	-	Lubricant flow rate into journal

The P&W test rig uses National Instruments LabVIEW 8.6® for data acquisition and shaker control. A custom made data acquisition program developed in Ref. [38] is modified for use in the test rig.

The user defines a vector of frequencies and the orbit amplitude in X and Y directions. The program generates a single frequency voltage control signal to excite the shakers, when the required condition is reached the program automatically records the different signals. Ref. [39] describes in detail the data acquisition code.

III.2 Lubricant supply system

Figure 11 shows a schematic of the lubricant delivery system. Oil is pumped from a sump tank of 150 liter capacity into the test rig via a frequency controlled pump. In the lubricant supply line before entering the test rig, measurements of oil inlet flow rate and pressure are registered. A relief valve limits the pressure in the supply line. At a maximum pressure of 6.2 bar, the valve opens and routes the oil back to the sump tank.

After entering the test rig, oil exits from the top and bottom damper film lands, into two return lines connected to a secondary pump that suctions the oil back into the oil reservoir.

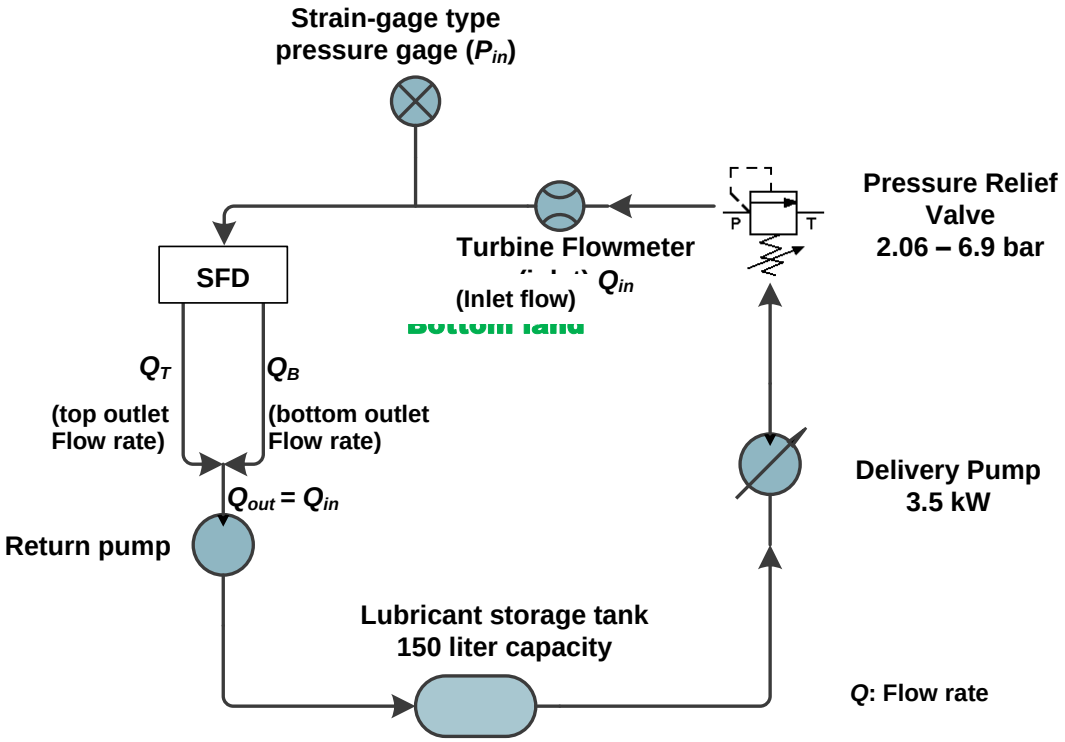

Figure 11. Schematic view of lubrication system [39]

CHAPTER IV

LUBRICANT PROPERTIES AND MEASUREMENT OF FLOW RATES

The test rig operates with lubricant ISO VG 2 grade oil. At room temperature lubricant ISO VG 2 has the same viscosity properties as Mobil Jet oil II has at high temperatures; simulating the lubricant properties of a SFD in an aircraft engine.

IV.1 Density

The lubricant density is determined at an ambient temperature of 25^{o}C by weighing a known volume (1 liter) of lubricant oil. The oil density obtained is ρ=785 ± 0.5 kg/m^3.

IV.2 Viscosity

The lubricant viscosity (μ) is measured at increasing temperatures using a rotary viscometer. Figure 12 shows the measured viscosity versus lubricant temperature. The ASTM standard viscosity-temperature relation is

$$\mu = \mu_R e^{-\alpha_v (T - T_R)} \tag{1}$$

where (μ_R, T_R)=(2.96 cPoise, 25.2^{o}C) are a reference viscosity and temperature, respectively. The oil viscosity coefficient (α_v) is obtained from two measurements of viscosity and temperature as

$$\alpha_v = -\frac{\ln(\mu_2 / \mu_R)}{(T_2 - T_R)} = 0.0187 \frac{1}{^{\circ}C} \tag{2}$$

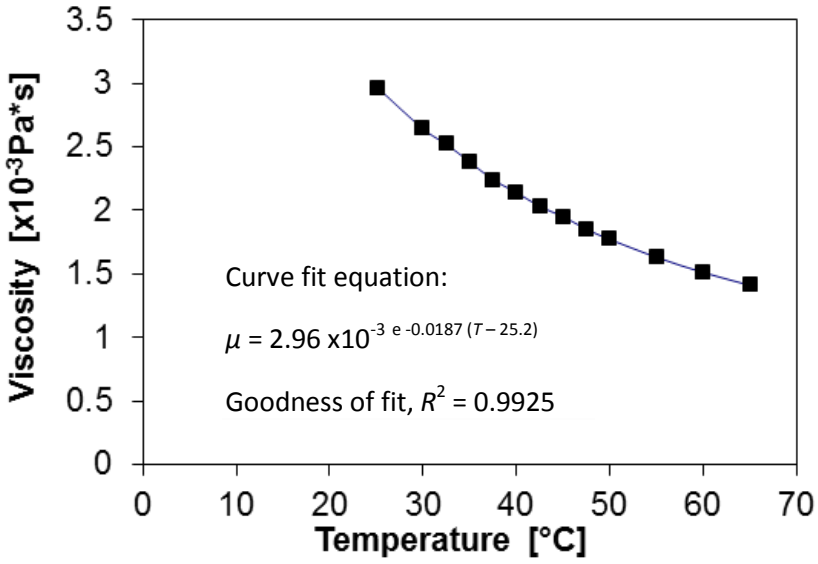

Figure 12. Measured viscosity versus temperature, Mobil Velocite 3 (ISO VG 2) oil [40]

The rotary viscometer manufacturer specifies accuracy of 10μPa·s, thus the uncertainty of the measurement is ±0.5 μPa·s. At room temperature (25°C) the lubricant viscosity is $\mu = (2.96 \pm 0.005) \times 10^{-3}$ Pa·s.

IV.3 Flow rate measurements

Figure 13 presents a hydraulic circuit representing the flow path of the lubricant inside the test damper with end seals. The lubricant enters the damper section at inlet pressure P_{in} and flow rate Q_{in}. After flowing through the three radial orifices (spaced 120° apart) with fluidic resistance R_o, the lubricant enters the central groove at pressure P_G. The lubricant streams, Q_T and Q_B, pass through the top and bottom film lands, respectively. Finally, each stream flows across the end seals at the top and bottom film lands, with resistances R_{TS} and R_{BS}, and discharges at ambient pressure P_a= 0 (gauge) [41]. Note that when operating as an open ends configuration (no seals installed), R_{TS} and R_{BS} equal zero.

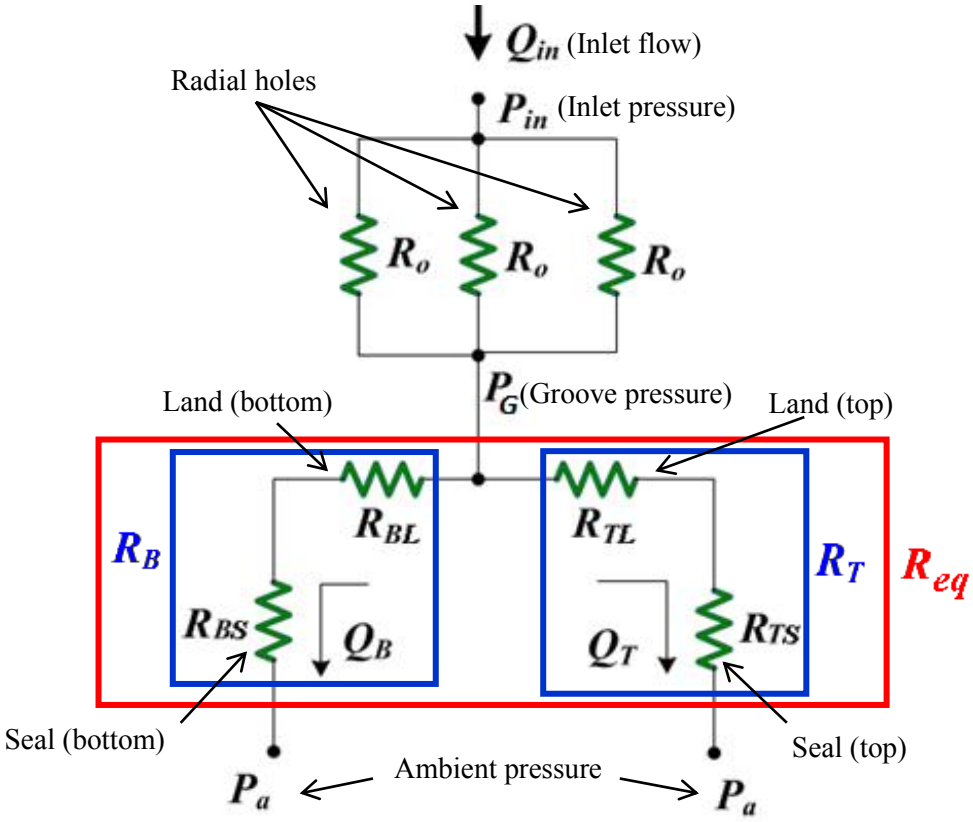

Figure 13. Hydraulic circuit diagram for sealed damper configuration [41]

During the measurements, the BC is centered (e_S = 0) and the damper lands are flooded with ISO VG2 lubricant at ~25°C. The inlet flow rate (Q_{in}) and the bottom outlet flow rate (Q_B) are measured for increasing groove pressures (P_G). The bottom flow rate is estimated by recording the time needed for the lubricant to fill a set volume (V=0.17±0.019 liters) while inlet flow rate is measured with a turbine flow meter of accuracy ±5%.

The film lands fluidic resistances (bottom and top) R_{BL} and R_{TL} are determined from flow rate measurements with the open ends damper configuration [39].

Then, the piston rings are installed in the top and bottom film lands. The piston rings have two slits closing ends, hence the lubricant exits the damper lands in a localized

region rather than evacuating evenly around the piston ring circumference. Flow rate measurements with the sealed ends configuration serve to determine the seals fluidic resistance R_{BS} and R_{TS}. For the top and bottom film land sections, the land and end seal fluidic resistances are in series. Hence[1],

$$Q_T = \frac{P_G - P_a}{R_{TL} + R_{TS}} = \frac{P_G}{R_T} = C_T P_G \; ; \; Q_B = \frac{P_G - P_a}{R_{BL} + R_{BS}} = \frac{P_G}{R_B} = C_B P_G \tag{3}$$

Note that only the equivalent (C_{eq}) and bottom (C_B) can be determined from flow rate measurements with the sealed damper. The fluidic resistances of the seals alone (R_{TS}, R_{BS}) are determined from the relations

$$\begin{aligned} R_{BS} &= \frac{1}{C_B} - \frac{1}{C_{BL}} \\ R_{TS} &= \frac{1}{C_T} - \frac{1}{C_{TL}} = \frac{1}{C_{eq} - C_B} - \frac{1}{C_{TL}} \end{aligned} \tag{4}$$

Figure 14 depicts the oil flow rate measurements at various groove pressures (P_G) for the open and end sealed configurations of the short and long dampers. The figure shows the flow conductances ($C=Q/P_G$) derived from a linear curve-fit of the test data. In general, $Q_b \sim 0.5 Q_{in}$ indicating that the top and bottom film lands offer nearly the same flow resistance. Similarly for the top and bottom end seals.

For the two damper configurations (short and long dampers) Table 2 summarizes the conductances of the film lands and the end seals for the top and bottom sections determined from flow rate measurements.

Table 2. Seal and land fluidic conductances (top and bottom) for the two dampers

Conductance (LPM/bar)	Journal B		Journal A	
	Bottom	Top	Bottom	Top
Land	8.87	9.7	4.59	5.33
Seal	1.69	1.10	0.13	0.17

[1] Recall that $R=1/C$ where C denotes flow conductance

Theoretically the axial flow rate in a centered open ends SFD without feed holes is [1]

$$Q = \frac{\pi D c^3}{12\mu_{(T)}} \frac{\Delta P}{L} \tag{5}$$

Hence the theoretical ratio between the two open ends configuration conductances is

$$\frac{C_{Long}}{C_{Short}} = \left(\frac{{c_A}^3 / L_A}{{c_B}^3 / L_B} \right)^3 = 1.87 \tag{6}$$

Note that the long damper land's conductance is ~1.9 times larger than the short damper and agrees well with Eq. (4).

Since the same piston ring seals are used in both sealed damper tests (short and long dampers) the seal coefficient is expected to be constant. However, the long damper configuration test data reveals an end seal fluidic resistance ~10 times larger than data from test on the short damper.

To explain the discrepancy, additional testing by following students will be required, a more detailed series of flow rate measurements that can lead to explain this behavior is required i.e., a larger range of pressures vs. flow rate. At present the results are adequate to use in the predictive code.

(a) Short length damper, *L*=12.7mm

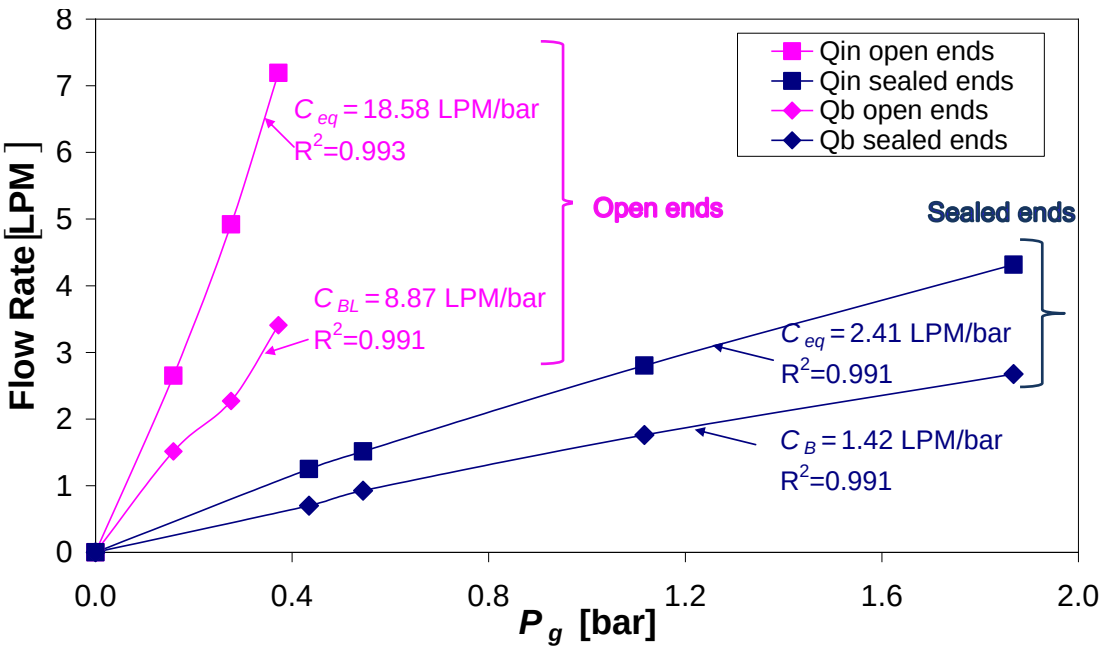

(b) Long damper, *L*=25.4mm

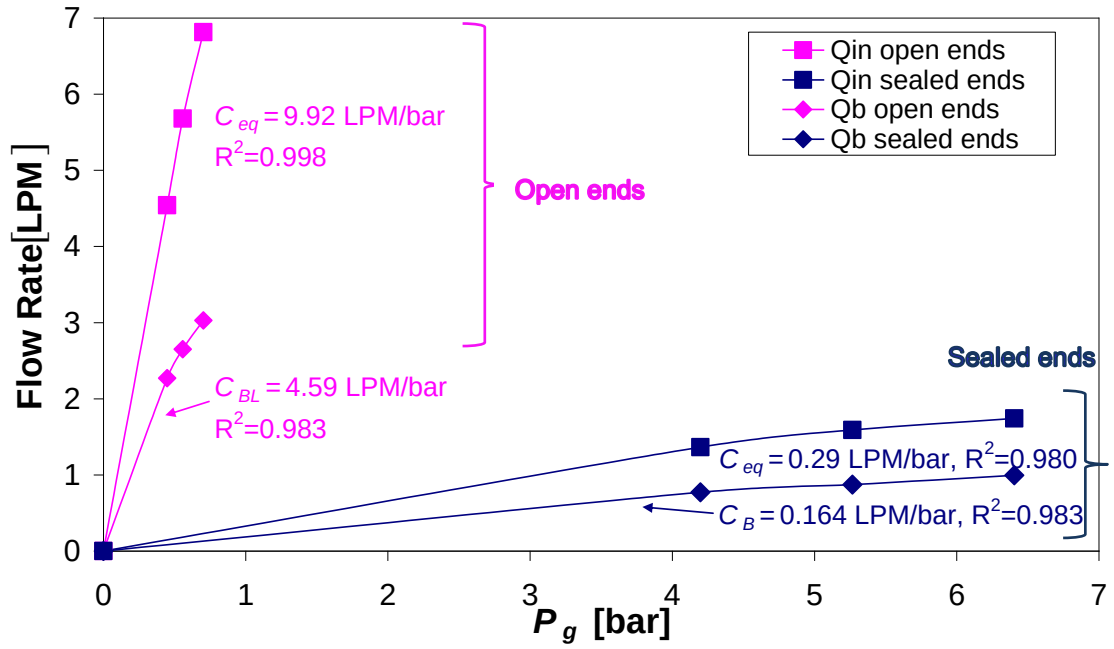

Figure 14. Flow rates versus central groove pressure for the open and sealed ends configurations of the (a) short length SFD and (b) long SFD

CHAPTER V

IDENTIFICATION OF SFD DAMPING AND ADDED MASS COEFFICIENTS

With the damper free of lubricant, i.e., under dry conditions, static pull tests are conducted on the system to determine the support stiffness K_S. The effective mass of the BC, M_{BC}, is estimated before assembling by weighing the rods and the BC with the instrumentation and attachments installed.

Next, periodic (single frequency) load tests are performed to identify the system structural stiffness $(K_s)_{X,Y}$, effective mass $(M_s)_{X,Y}$, and remnant damping $(C_s)_{X,Y}$ coefficients. The shakers deliver single frequency loads along X and Y axes to generate either circular or unidirectional motions of the BC. A DAQ code controls the excitation force at each frequency to maintain constant amplitude of motion defined by the rig operator.

The test rig is flooded with ISO VG 2 grade lubricant. Lubricant flow measurements into and out of the test section serve to confirm equal flow through the two parallel film lands; and in conjunction with static pressure measurements at the groove, serve to determine the resistance of the film lands. Reference [39] details flow rate measurements with the open ends dampers.

Then, the same dynamic load test procedure used on the dry structure is performed on the lubricated system to determine the lubricated system coefficients; stiffness (K), damping (C) and mass (M), for an open ends configuration.

Next, piston rings are carefully installed on a journal end grooves. Flow rate measurements, following the same procedure as with the open ends configuration, serve to determine flow resistances of the two end sealed film lands. A simple flow analysis renders the flow conductance of the end seals alone (see prior Chapter). Figure 15 shows a cross section view of the SFD with the piston rings installed illustrating the lubricant flow path throw the damper film lands.

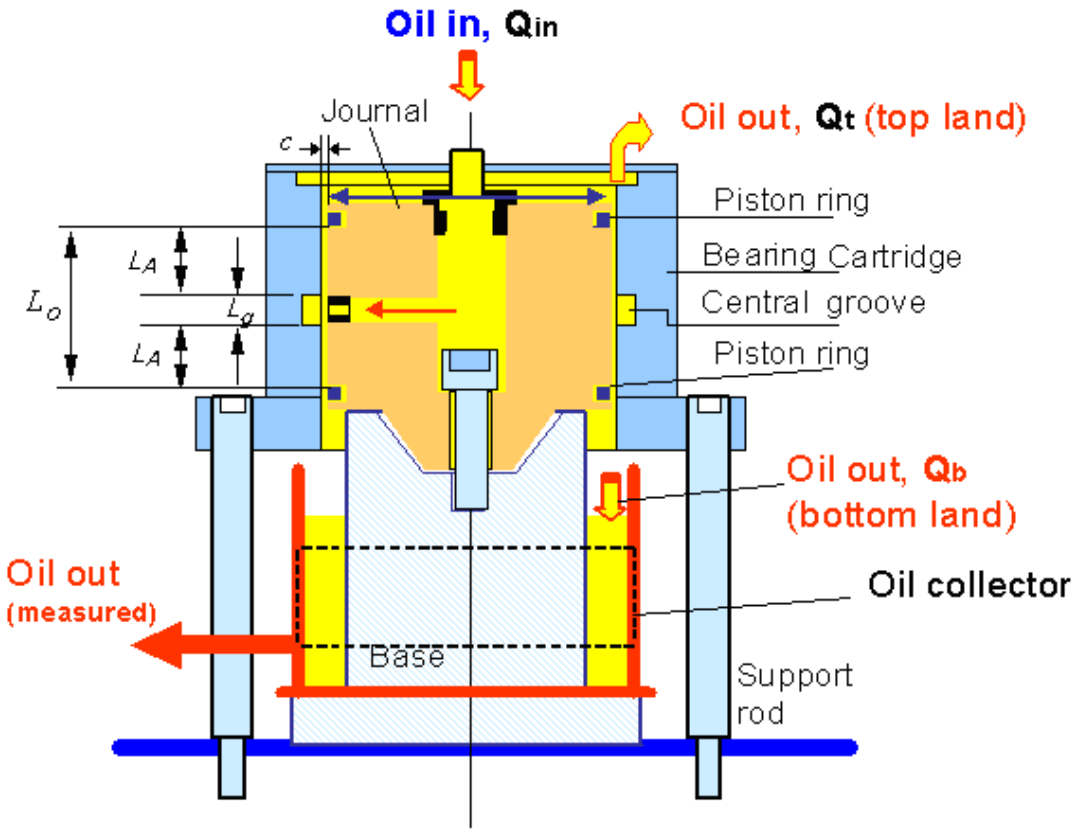

Figure 15. Cross section view of long SFD test rig and lubricant flow path through damper film lands (Journal A with piston rings installed)[41]

Circular orbit tests on the sealed damper, at centered and off-centered BC eccentricities, serve to determine the sealed lubricated system coefficients (*K, C, M*). The Instrument Variable Filter Method (IVFM) [42]extracts the mechanical parameters of the dry and lubricated test system: stiffness, damping and inertia force coefficients.

Finally, the force coefficients of the SFD alone are determined by subtracting the dry system coefficients from the lubricated system coefficients. In matrix form

$$(\mathbf{K, C, M})_{SFD} = (\mathbf{K, C, M}) - (\mathbf{K, C, M})_s \qquad (7)$$

where the suffix SFD refers to the squeeze film alone. Above **K**, **C** and **M** denote the matrices of four stiffness, four damping and four mass coefficients, respectively.

The test structure is considered as a two degree of freedom mechanical system, as shown in Figure 16. Hence, two linearly independent excitation force vectors that render

two linearly independent displacement vectors are enough to determine the mechanical parameters of the system.

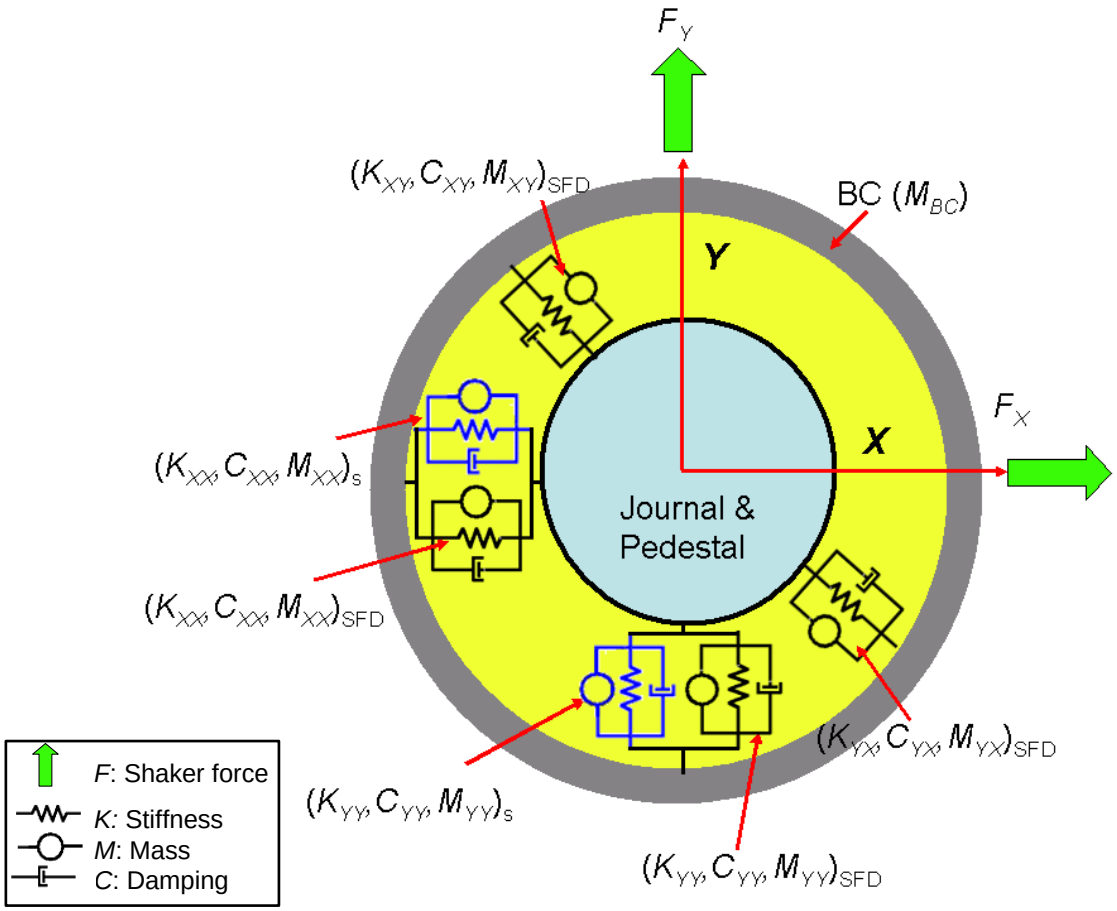

Figure 16. Schematic representation of force coefficients from test SFD and rig support structure [43][2]

At centered or off-centered static positions of the BC, and for the dry and lubricated systems, controlled single frequency loads ($F_{X(t)}$, $F_{Y(t)}$) exerted on the BC produce either unidirectional, circular or elliptic whirl motions.

To obtain unidirectional displacements of the BC, excitation loads are imposed in the *X* axis while the *Y* shaker is inactive, and vice versa. The load vectors are

[2] The schematic has been modified from the reference to represent a SFD.

$$\mathbf{F}^1 = \begin{bmatrix} F_{X_{(t)}} \\ 0 \end{bmatrix}; \quad \mathbf{F}^2 = \begin{bmatrix} 0 \\ F_{Y_{(t)}} \end{bmatrix} \tag{8}$$

To generate circular orbital motions of the BC relative to the journal, two single frequency loads, along the *X* and *Y* axes, are imposed on the BC. In general $|F_X|=|F_Y|$ and with phase difference of $+90^o$ and -90^o induce forward and backward circular whirl motions. The load vectors are

$$\begin{aligned} \mathbf{F}^1 &= \begin{bmatrix} F_X{}^1 \cos(\omega t) \\ -F_Y{}^1 \sin(\omega t) \end{bmatrix} = \mathrm{Re}\left(\begin{bmatrix} F_X{}^1 \\ iF_Y{}^1 \end{bmatrix} e^{i\omega t} \right) \\ \mathbf{F}^2 &= \begin{bmatrix} F_X{}^2 \cos(\omega t) \\ -F_Y{}^2 \sin(\omega t) \end{bmatrix} = \mathrm{Re}\left(\begin{bmatrix} F_X{}^2 \\ -iF_Y{}^2 \end{bmatrix} e^{i\omega t} \right) \end{aligned} \tag{9}$$

The reaction forces of the squeeze film damper are modeled as

$$-\mathbf{F_{SFD}} = \mathbf{M_{SFD}}\ddot{\mathbf{z}} + \mathbf{K_{SFD}}\mathbf{z} + \mathbf{C_{SFD}}\,\dot{\mathbf{z}} \tag{10}$$

The equation of motion for the dry test system is

$$M_{BC}\,\mathbf{a} + \mathbf{K_s}\,\mathbf{z} + \mathbf{C_s}\,\dot{\mathbf{z}} + \mathbf{M_s}\,\ddot{\mathbf{z}} = \mathbf{F} \tag{11}$$

where $\mathbf{a}=(a_X, a_Y)^T$ is the acceleration vector of the BC, $\mathbf{z} = (x, y)^T$ is the vector of BC displacements relative to the journal, and $\mathbf{F}=(F_X,F_Y)^T$ is the vector of applied external loads. M_{BC} is the BC effective mass. $\mathbf{K_s}$, $\mathbf{C_s}$ and $\mathbf{M_s}$ are the structure support stiffness matrix, remnant damping matrix, and residual mass[3] matrix, respectively.

In the frequency domain, the test system equation of motion becomes

$$\left[\mathbf{K_s} - \omega^2\,\mathbf{M_s} + i\,\omega\mathbf{C_s}\right]\bar{\mathbf{z}} = \bar{\mathbf{F}}_M = \bar{\mathbf{F}} - M_{BC}\,\bar{\mathbf{a}} \tag{12}$$

where $\bar{\mathbf{z}}_{(\omega)}=DFT(\mathbf{z}_{(t)})$, $i\omega\bar{\mathbf{z}}_{(\omega)}=DFT(\dot{\mathbf{z}}_{(t)})$, $\bar{\mathbf{F}}_{(\omega)}=DFT(\mathbf{F}_{(t)})$, and $\bar{\mathbf{a}}_{(\omega)}=DFT(\mathbf{a}_{(t)})$ (13)

are the discrete Fourier transforms (DFT) of the time signals. The mechanical impedance of the dry test system is

$$\mathbf{H}_{dry} = \left[\mathbf{K_s} - \omega^2\,\mathbf{M_s} + i\,\omega\mathbf{C_s}\right] \tag{14}$$

[3] The matrix **M**s corresponds to a residual mass matrix of small values, since the mass of the system is considered in the term $M_{BC}\mathbf{a}$.

When the damper lands are flooded with lubricant, the forced response includes both the structure response and the squeeze film damper response. The EOMs for the lubricated system are

$$M_{BC}\,\mathbf{a}+\left(\mathbf{M_s}+\mathbf{M_{SFD}}\right)\ddot{\mathbf{z}}+\left(\mathbf{K_s}+\mathbf{K_{SFD}}\right)\mathbf{z}+\left(\mathbf{C_s}+\mathbf{C_{SFD}}\right)\dot{\mathbf{z}}=\mathbf{F} \tag{15}$$

where $\mathbf{M_{SFD}}$, $\mathbf{K_{SFD}}$ and $\mathbf{C_{SFD}}$ are the SFD mass, stiffness, and viscous damping matrices, respectively. In the frequency domain Eq. (10) becomes

$$\left[\left(\mathbf{K_s}+\mathbf{K_{SFD}}\right)+i\,\omega\left(\mathbf{C_s}+\mathbf{C_{SFD}}\right)-\omega^2\left(\mathbf{M_{SFD}}+\mathbf{M_s}\right)\right]\bar{\mathbf{z}}=\bar{\mathbf{F}}_M=\bar{\mathbf{F}}-M_{BC}\,\bar{\mathbf{a}} \tag{16}$$

Define the mechanical impedance of the lubricated system as

$$\mathbf{H}=\mathbf{H_{dry}}+\mathbf{H_{SFD}}=\mathbf{K}+i\,\omega\mathbf{C}-\omega^2\mathbf{M} \tag{17}$$

where $\mathbf{K}=\mathbf{K_s}+\mathbf{K_{SFD}}$; $\mathbf{C}=\mathbf{C_s}+\mathbf{C_{SFD}}$; $\mathbf{M}=\mathbf{M_{SFD}}+\mathbf{M_s}$ are the stiffness, damping and mass matrices of the lubricated system.

On substituting Eq.(15) into Eq.(14), the equations of motion in algebraic form in the frequency domain are

$$\begin{aligned}\mathbf{H}\bar{\mathbf{z}}^1&=\bar{\mathbf{F}}_M{}^1\\ \mathbf{H}\bar{\mathbf{z}}^2&=\bar{\mathbf{F}}_M{}^2\end{aligned} \tag{18}$$

Stacking Eqs. (16)

$$\mathbf{H}\left[\bar{\mathbf{z}}^1\;\;\bar{\mathbf{z}}^2\right]=\left[\bar{\mathbf{F}}_M{}^1\;\;\bar{\mathbf{F}}_M{}^2\right] \tag{19}$$

Eq. (17) can be written as

$$\mathbf{H}=\begin{bmatrix}H_{XX} & H_{XY}\\ H_{YX} & H_{YY}\end{bmatrix}=\left[\bar{\mathbf{F}}_M{}^1\;\;\bar{\mathbf{F}}_M{}^2\right]\left[\bar{\mathbf{z}}^1\;\;\bar{\mathbf{z}}^2\right]^{-1} \tag{20}$$

A first estimate of the system parameters $(K, C, M)_{i,j=X,Y}$ is determined by curve fitting the discrete set of impedances $(H_{XX}, H_{YY}, H_{XY}, H_{YX})_{k=1,2....Nfreq}$, one set for each frequency ω_k, to the analytical model [43]

$$\mathrm{Re}(H_{XX})\rightarrow K_{XX}-\omega^2 M_{XX};\;\;\mathrm{Im}(H_{XX})\rightarrow\omega\,C_{XX} \tag{21}$$

The IVFM, a frequency domain parameter identification method that iterates the least-squares approximation to reduce the estimation error (noise), is used to determine the test system force coefficients. The IVFM uses the flexibility matrix $\mathbf{G} = \mathbf{H}^{-1}$ rather

than directly curve fitting the mechanical impedances. Note that **GH = I**, the identity matrix; however, due to measurement noise or procedure noise there is always an error (**e)**, i.e.,

$$\mathbf{G}\,\mathbf{H} = \mathbf{G}\left[\mathbf{K} - \omega^2\mathbf{M} + i\omega\mathbf{C}\right] = \mathbf{I} + \mathbf{e} \tag{22}$$

Minimization of the error (**e)** leads to the final identification equation

$$\begin{bmatrix} \underline{\mathbf{M}} \\ \underline{\mathbf{C}} \\ \underline{\mathbf{K}} \end{bmatrix} = \left(\underline{\mathbf{A}}^{\mathbf{T}}\underline{\mathbf{A}}\right)^{-1}\underline{\mathbf{A}}^{\mathbf{T}}\underline{\mathbf{I}} \tag{23}$$

where $\mathbf{A}^k = \mathbf{G}^k\left[\mathbf{I} \vdots -\omega_k{}^2\mathbf{I} \vdots i\omega_k\mathbf{I}\right]$. Eq. (19) is a typical least-squares error estimator.

$$\begin{bmatrix} \underline{\mathbf{M}} \\ \underline{\mathbf{C}} \\ \mathbf{K} \end{bmatrix}^{m+1} = \left([\mathbf{W}^{(m)}]^{\mathbf{T}}\mathbf{W}^{(m)}\right)^{-1}[\mathbf{W}^{(m)}]^{\mathbf{T}}\mathbf{I} \tag{24}$$

A first iteration (m=1) is performed with $\mathbf{W}^1$=**A**, which corresponds to the standard least-squares solution of the problem, eq. (21). Then, Eq. (22) is applied iteratively until a given convergence criterion or tolerance is satisfied [43].

The identified parameters are constant and valid within a selected frequency range. The procedure assumes the mechanical system is linear. Ref. [43] presents a more comprehensive explanation of the parameter identification method.

CHAPTER VI

IDENTIFICATION OF TEST STRUCTURE PARAMETERS

VI.1 Static pull test

Twelve rods support the BC and provide structural stiffness. Figure 17 depicts a schematic top view of the disposition of the support rods relative to the (*X*,*Y*) coordinate system; blue circles represent the 4 main support rods and the green circles represent the 8 flexural rods installed to give additional stiffness to the test system.

With the damper free of lubricant and the piston rings installed, static pull tests are conducted to determine the support stiffness K_S. The static loader, located 45^o away from the *X* and *Y* axes, displaces the BC. A load cell records the applied force, and eddy current sensors, mounted in the BC, along *X* and *Y* axis, measure the BC displacement relative to the journal. Figure 18 shows the loads and the resultant displacements. The static stiffness K_S~18.7 MN/m follows from a linear curve-fit of the test data. Note the linearity of the load versus displacement relation showing that the piston rings do not impair the BC displacement. That is, the piston rings' inner diameters (ID_s) are larger than the journal's diameter at the seals groove locations, D_J [41]. The static stiffness is independent of the installed journal; thus, this type of test is performed only once.

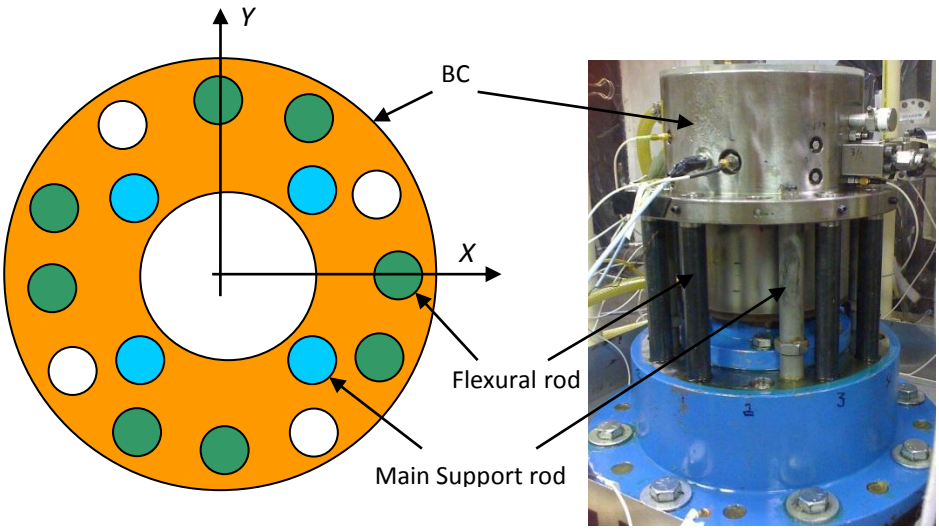

Figure 17. Disposition of 12 support rods holding bearing cartridge

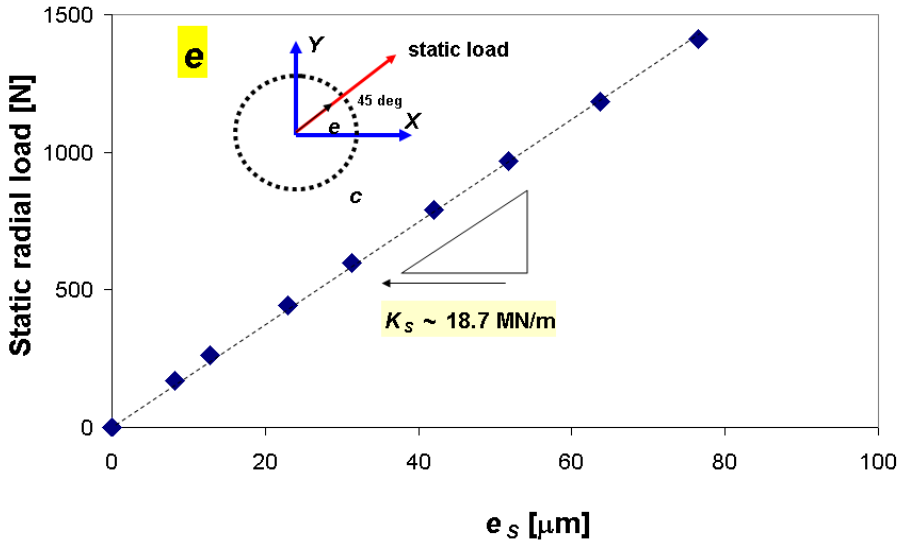

Figure 18. Static load vs. BC displacement from pull tests on BC (12 rods installed)

Before assembly, the mass of the BC along with the instrumentation and attachments are weighed. The mass of the bearing cartridge equals 17.6 kg. The flexural rods are 0.45 kg each; the rods behave as cantilever beams and contribute with ¼ of their mass [44]. Thus, the effective mass of the test system (M_{BC}) is 18.5 kg.

VI.2 Dry test system coefficients identified from single frequency load tests

On the dry damper (no lubricant) with piston rings installed, single frequency load tests are performed on the centered BC (e_S=0) to identify the system structural stiffness $(K_s)_{X,Y}$, residual mass $(M_s)_{X,Y}$, and remnant damping $(C_s)_{X,Y}$ coefficients. The shakers deliver loads along the X and Y axes to generate circular motions of the BC with an amplitude of $r<0.01c$.

Dry tests are performed in both damper configurations. For the short length damper the structure parameters are identified from circular centered orbits (CCOs) of amplitude $r=0.055c_B$ (7.56 μm) and for frequencies from 50 to 210 Hz. For the long damper CCOs of amplitude $r=0.054c_A$ (7.61 μm) and excitation frequencies from 110 to 220 Hz serve to determine the structure parameters.

The IVFM, described in Chapter V, serves to identify the dry system parameters from the ensuing flexibility functions $\{G_{ij}\}_{i,j=X,Y}$. Figure 19 shows the amplitude of the flexibility functions derived experimentally and the respective flexibility functions built with the identified parameters for test on the short and long dampers, the vertical lines denote the starting and ending frequencies for parameter identification (f_{start}) and (f_{end}), respectively. Note that the flexibility functions include the structural stiffness (K_s), the residual mass (M_s), and the remnant damping (C_s). The force from the structural stiffness overwhelms the forces arising from the residual mass and remnant damping; and hence, the flexibility function is a near straight line over the test frequency range.

The estimated mass of the system is M_{BC}=19 kg. However, by trial and error, the identification code shows better correlation with the experimental data when using M_{BC}= 21.8kg[4].

[4] The mass of the system is estimated with the assumption of a cantilever beam (fixed-free ends) vibrating in the first mode shape. But in reality the rods might be vibrating in a different mode shape changing the rods mass contribution.

a) Short SFD

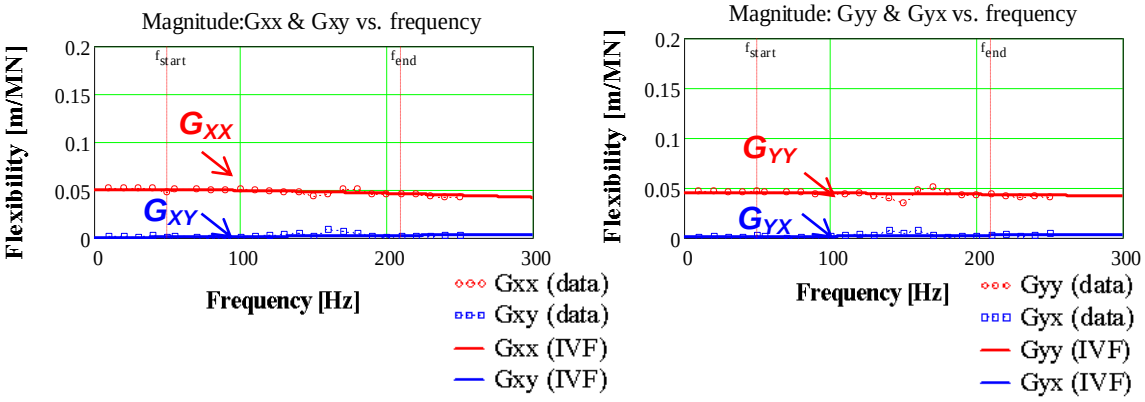

b) Long SFD

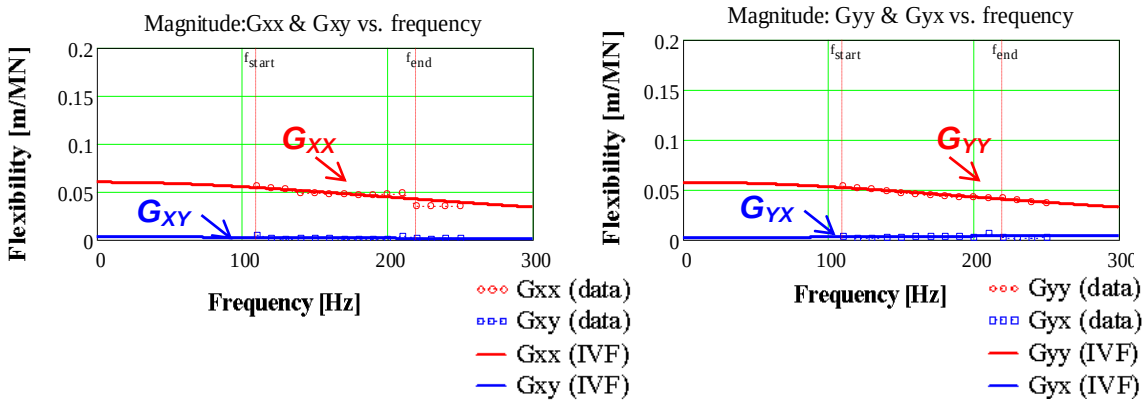

Figure 19. Dry test system: Amplitude of flexibility functions G_{ij} vs. excitation frequency for two sealed ends dampers. (a) Short length damper and (b) Long damper

Table 3.a and 3.b lists the identified force coefficients for the short length and long damper structures, respectively, including the system's natural frequency (f_n) and damping ratios (ξ_s).

$$f_n = \frac{1}{2\pi}\sqrt{\frac{K_s}{M_{BC}}} \qquad \xi_s = \frac{C_s}{2M_{BC}\omega_n} \tag{25}$$

Note that the structural parameters are independent of the installed journal. For both configurations, the estimated stiffness for the dry system (K_s) from dynamic load tests is within 10% of the static parameter (K_S).

As expected, the remnant damping (C_s) is very small. The remnant damping determines the system viscous damping ratios (ξ_s). For the short length damper the damping ratio (ξ_s) is ~3% along *X* direction and ~5% along the *Y* direction. For the long damper, the damping ratio (ξ_s) is ~7% along the *X* and ~4% in the *Y* directions. These magnitudes are typical for steel structures [35]. The magnitudes of the cross-coupled stiffness coefficients are very low, denoting a nearly isotropic system.

Table 3. Structural parameters of dry test system for two sealed ends SFD configurations. Derived from CCOs. Identified by the IVF method. K_S=18.7MN/m and M_{BC}=21.8kg

a) Short length damper. Frequency range 50 Hz- 210 Hz

Dynamic coefficients		Direct ***XX***	Direct ***YY***	Cross ***XY***	Cross ***YX***
Stiffness	K_s [MN/m]	19.6	21.6	0.2	0.2
Residual Mass	M_s [kg]	-1.1	-0.5	0.3	0.3
Remnant Damping	C_s [kN-s/m]	1.3	1.9	0.3	0.4
Natural frequency	f_n [Hz]	147.4			
Damping ratio	ξ_s	0.03	0.05		

b) Long damper. Frequency range 110 Hz- 220 Hz

Dynamic coefficients		Direct ***XX***	Direct ***YY***	Cross ***XY***	Cross ***YX***
Stiffness	K_s [MN/m]	16.7	17.4	0.8	0.6
Residual mass	M_s [kg]	-3.5	-3.7	0.3	-0.8
Remnant damping	C_s [kN-s/m]	2.9	1.8	0.6	0.2
Natural frequency	f_n [Hz]	147.4			
Damping ratio	ξ_s	0.07	0.04		

CHAPTER VII

IDENTIFICATION OF FORCE COEFFICIENTS FOR LUBRICATED SYSTEM AND SFD

VII.1 Identification of lubricated system coefficients

After completion of tests with the dry structure, the test system with piston rings installed is flooded with ISO VG2 lubricant at ~25C^{o}. The lubricant enters the groove with flow rate Q_{in} and at static pressure P_G.

Note that the high structural stiffness and large squeeze film damping, coupled with the limit load capacity of the shakers (2,200N), restricts the maximum BC displacements to within 20% of the bearing radial clearance. In addition, Ref. [39] demonstrates that on the current test damper, open ended, the SFD damping and added mass coefficients remain nearly constant when operating at amplitudes of motion r/c<0.20. Therefore, dynamic load tests are performed at only one (r) amplitude for each damper.

Dynamic load tests are conducted at the centered condition and at various static eccentricities (e_S) along the static loader direction (45^{o} away from the X and Y axes). Table 4 lists the SFD geometry, the operating conditions, and the lubricant properties for circular orbit tests on the long and the short sealed ends damper configurations.

Table 4. Summary of SFD geometry, operating conditions and fluid properties for test with the lubricated test system. Sealed ends configuration.

SFD geometry	Long journal (A)	Short journal (B)
Journal diameter	D=12.7cm	
Damper axial length (groove + 2 lands)	5L=63.5 mm	3L=38.1 mm
Radial land clearance	c_A=141.0 μm	c_B=137.9 μm
Central groove length	L_G=12.7mm	

Table 4. Continued

SFD geometry	**Long journal (A)**	**Short journal (B)**
Central groove depth	d_G=9.525 mm	
Operating conditions	**Long journal (A)**	**Short journal (B)**
orbit amplitude (r)	$0.054c_A$	$0.055c_B$
Frequency range of identification	110-250 Hz	50-250 Hz
Eccentricity (e_S)	$0\text{-}0.36c_A$	$0\text{-}0.37c_B$
Effective mass (M_{BC})	21.8 kg	
Static stiffness (K_S)	18.7 MN/m	
groove pressure (P_G)	4.69 bar (gage)	0.76 bar (gage)
Inlet flow rate (Q_{in})	1.32 LPM	1.40 LPM
Fluid properties ISO VG2		
Supply temperature (T_{in})	25 ^{o}C	
Viscosity at T_{in} (μ)	0.00296 Pa·s	
Density (ρ)	785 kg/m^3	

Figure 20 illustrates the amplitude of the flexibility functions $|G_{ij}|$ for the two lubricated test system configurations at the centered position (e_S=0). The flexibility functions include the effects of the total stiffness (K_{SFD} + K_s), added mass and residual mass (M_{SFD} + M_s), and squeeze film viscous damping and remnant structural damping (C_{SFD}+C_S). The vertical lines in the figure indicate the start (f_{start}) and end (f_{end}) frequencies for parameter identification.

The lubricated system flexibility functions differ drastically from those of the dry system (Figure 19); the appearance of a significant added mass in the lubricated system flexibilities results in a distinctive peak, not observed in the dry system flexibility functions. Recall that the flexibility functions do not include the effect of the BC physical mass (M_{BC}), thus this peak is not denoting true resonant frequency.

Note that the *Y* intercepts of both dry and lubricated flexibility functions (Figures 19 and 20) are nearly the same. This denotes very similar stiffness magnitudes and evidencing that the squeeze film does not generate stiffness coefficients ($K_{SFD} \approx 0$)[5].

The squeeze film lands add viscous damping, resulting in a significant increase in damping ratios compared to those of the dry system. For the short length damper, the damping ratio increases from ξ_s=0.07 to ξ_{YY}=ξ_{XX} =0.26, and for the long damper the damping ratio increases from ξ_s=0.04 to ξ_{XX}=0.78 and ξ_{YY}=0.79.

Appendix A lists the identified direct and cross-coupled force coefficients for the lubricated dampers and Appendix B describes the uncertainty analysis for the acquired data. In general, for both short length and long damper configurations and for different static eccentricities, the cross coupled force coefficients are an order of magnitude smaller than the direct coefficients, thus considered negligible. The absence of significant cross-coupled damping coefficients, C_{XY} and C_{YX}, demonstrates that the SFD operates without gaseous or vapor lubricant cavitation[46].

Despite tests starting at 5 Hz, the parameter identification begins at f_{start}=50 Hz due to high noise levels in the acceleration signals at frequencies below 50 Hz. Hence, identification encompassing frequencies below 50 Hz will deliver erroneous coefficients.

For the sealed ends short length damper tested at the centered condition (e_S=0), Figure 21 illustrates the real and imaginary parts of the mechanical impedances from the test data and the respective impedances derived from the physical model, K_{ij}-$\omega^2 M_{ij}$ = Re (H_{ij}) and ωC_{ij}=Im(H_{ij}). The figure also denotes the goodness of physical model fits (R^2). In the figure the vertical lines indicate the parameter identification frequency range, f_{start} to f_{end}.

[5] Squeeze films do not generate stiffness coefficients, see Refs. [10,45]

a) Short length SFD

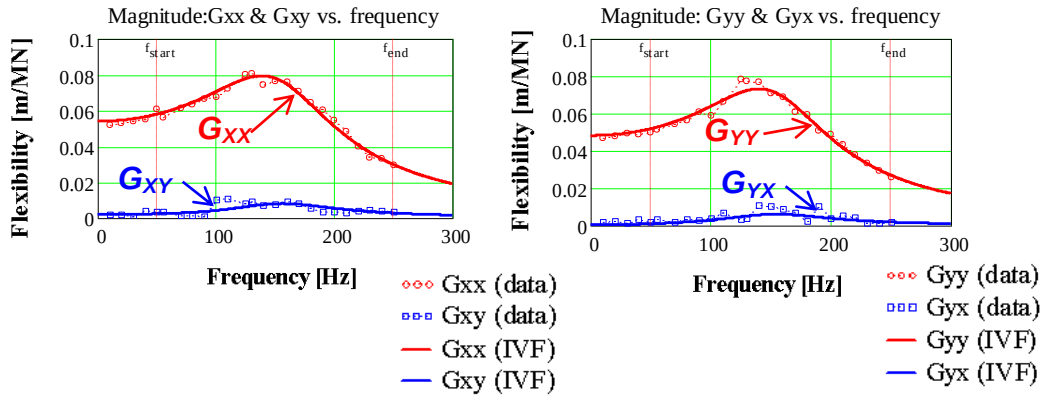

b) Long SFD

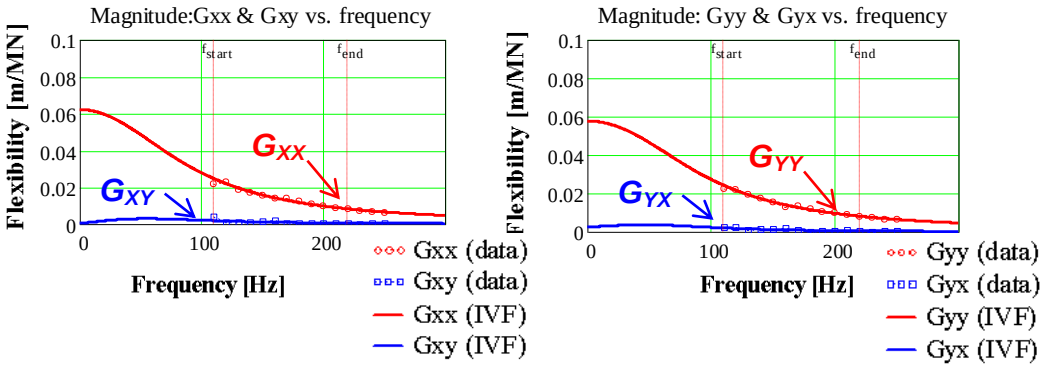

Figure 20. Lubricated test system: Amplitude of flexibility functions G_{ij} vs. excitation frequency for. Two sealed ends dampers (a) short journal and (b) long journal

In general, the goodness of physical model curve fits R^2 is >0.95 for both the real and imaginary parts of the mechanical impedance, indicating the adequacy of the physical model.

Appendix C lists the goodness of the curve fits for the estimated physical parameters $(K, C, M)_{i,j=X,Y}$. Experimental results for other eccentricities and from tests with the long damper are consistent and are not presented here for brevity.

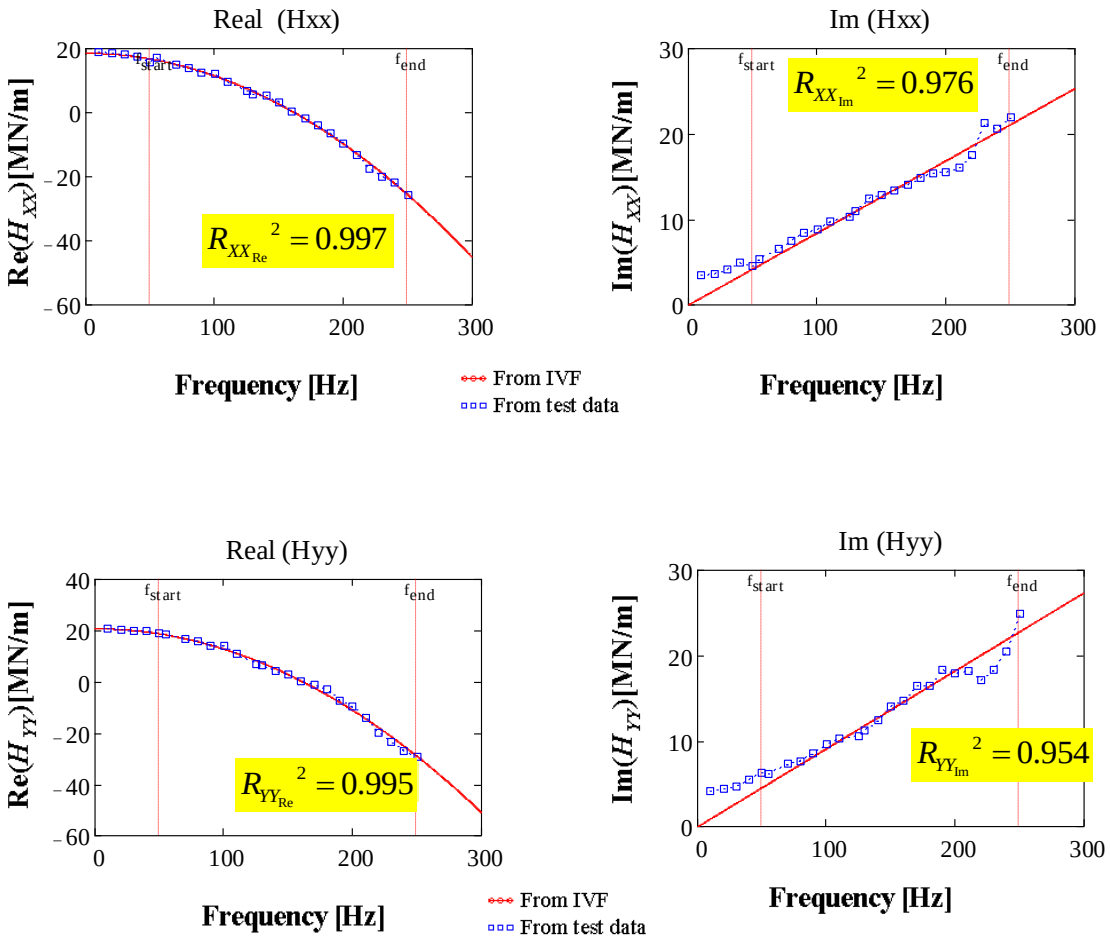

Figure 21. Lubricated test system: Real and imaginary parts of direct impedances (H_{XX} , H_{YY}) vs. excitation frequency. Experimental data and fits using identified parameters. Centered journal (e_S=0), circular orbits r =0.055c_B. Sealed ends short length damper. Goodness of fit (R^2) noted on each graph

Figure 22 illustrates the experimental direct damping coefficient for the short length damper, determined by dividing the imaginary part of the experimental impedances by the frequency (Im(H)/ω), and the damping coefficients advanced by the IVF method (C_{XX}, C_{YY}) versus the excitation frequency (ω). As expected for the identification range, the direct damping remains constant, indicating the absence of oil cavitation or air ingestion in the damper [46].

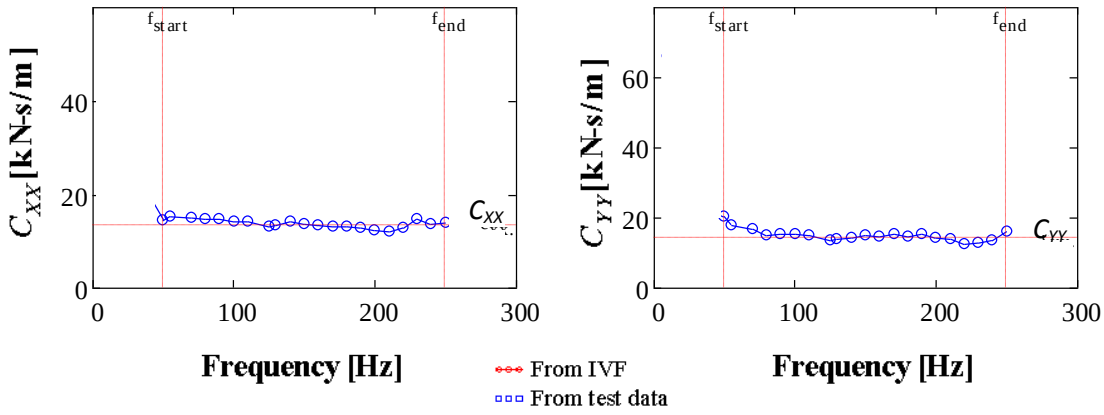

Figure 22. Lubricant test system: Imaginary part of system impedance divided by excitation frequency (H/ω) vs. excitation frequency and estimated damping coefficients (C_{XX}, C_{YY}). Sealed ends short length damper. CCOs of amplitude $r=0.055c_B$.

VII.2 Estimation of SFD force coefficients

The force coefficients for the squeeze film damper alone (two film lands in parallel separated by a central groove) are determined by subtracting the dry system force coefficients from the lubricated system ones, as in Eq. (3).

In general, the identified stiffness K_{SFD} is nearly zero, since a SFD does not generate stiffness even at the larger static eccentricities in both sealed ends configurations. As mentioned before, $K_S \approx K_s$ leading to $(K_{XX}, K_{YY})_{SFD} \approx 0$, this is expected since SFDs do not generate stiffness [10][6]. See appendix A for the data.

The SFD damping and added mass coefficients presented henceforth are normalized with respect to predictions derived from simple formulas for an open ends damper, as described in Appendix D. That is $\bar{C}=C/C^*$, $\bar{M}=M/M^*$. Table 5 lists the normalizing coefficients (C^*, M^*) for the short length and long dampers.

[6] A notable exception occurs for the long damper at the largest static eccentricity where significant direct and cross coupled stiffness coefficients are identified.

Table 5. Predicted normalizing force coefficients for two parallel film lands separated by a central groove [39]

Long damper Land length L_A=2.54 cm, clearance c_A=141.0μm	C_A^* (kN-s/m)	M_A^* (kg)
	6.798	2.985
Short length damper Land length L_B=1.27 cm, clearance c_B=137.9 μm	C_B^* (kN-s/m)	M_B^* (kg)
	0.918	0.386

Figure 23 depicts the test SFD direct damping $(\bar{C}_{XX},\bar{C}_{YY})_{\text{SFD}}$ and added mass coefficients $(\bar{M}_{XX}, \bar{M}_{YY})_{\text{SFD}}$ for the short length damper versus static eccentricity ratio (e_S/c_B), obtain from circular orbits of amplitude r=0.055c_B. The identification frequency range tests is 50 Hz to 250 Hz. Note the coefficients are normalized.

The identified direct added mass and damping coefficients remain nearly constant with varying static eccentricity (e_S) up to ~36% of the radial clearance. The sealed short length SFD offers ~15 times more damping and ~50 times more added mass than predictions from a simplified model for an open ends damper. The end seals aid to increase the damping. Recall, the simplified model does not account for the fluid flow interactions between the film lands and the central feed groove.

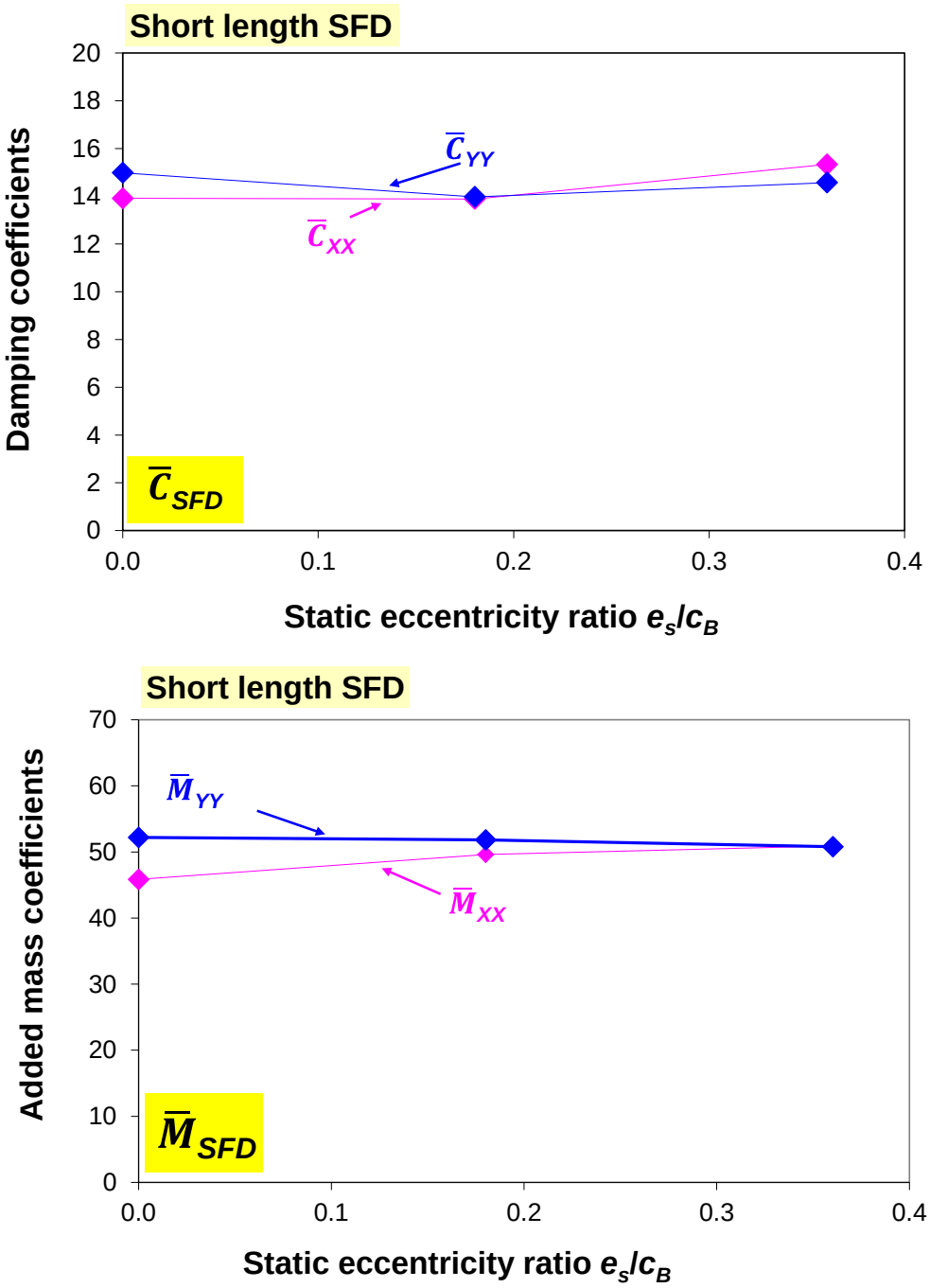

Figure 23. Short length sealed ends damper. Direct damping $(\bar{C}_{XX},\bar{C}_{YY})_{SFD}$ and added mass coefficients $(\bar{M}_{XX}, \bar{M}_{YY})_{SFD}$ versus static eccentricity ratio (e_S/c_B). Test data obtained from circular orbits of amplitude r=0.055c_B

The cross coupled damping coefficients $(C_{XY,}\ C_{YX})_{SFD}$ increase moderately with static eccentricity, being at least an order of magnitude lower than the direct damping coefficients, thus considered negligible and not herby presented. Appendix A lists the identified direct and cross-coupled force coefficients for the two dampers.

For the sealed ends long damper, Figure 24 illustrates the identified SFD damping and added mass coefficients versus the static eccentricity ratio (e_S/c_A). The direct damping coefficients increase slightly with the eccentricity ratio, while the added mass coefficients seem to first decrease and then increase with increasing eccentricity ratio.

The results for the sealed long damper are similar to those for the sealed short length dampers, the added mass and the damping coefficients are large when compared to a simplified open ends formula. Recall that the normalizing coefficients are different for the short length and long dampers. In general $\bar{C}_{XX} \sim \bar{C}_{YY}$ denoting the viscous damping has isotropic features.

The added mass initially decreases and then increases with static eccentricity (up to ~$0.4c_A$) and is ~22 times larger than predictions from a simplified formula for the open ends damper, evidencing that the groove does not isolate the squeeze film lands but, contrary to common knowledge, it generates large dynamic pressures, i.e., large fluid inertia reaction forces [35].

The damping coefficient increases slightly with static eccentricity and is ~9 times larger than predictions from a simplified formula for an open ends SFD. The large difference evidence the effectiveness of the seals in increasing the damping and the contribution of the central feed groove in the SFD performance. Chapter IX compares experimental results for the sealed ends damper to those of the open ends dampers [39], and hence identify the individual contributions of the seals and the central feed groove to the SFD damping.

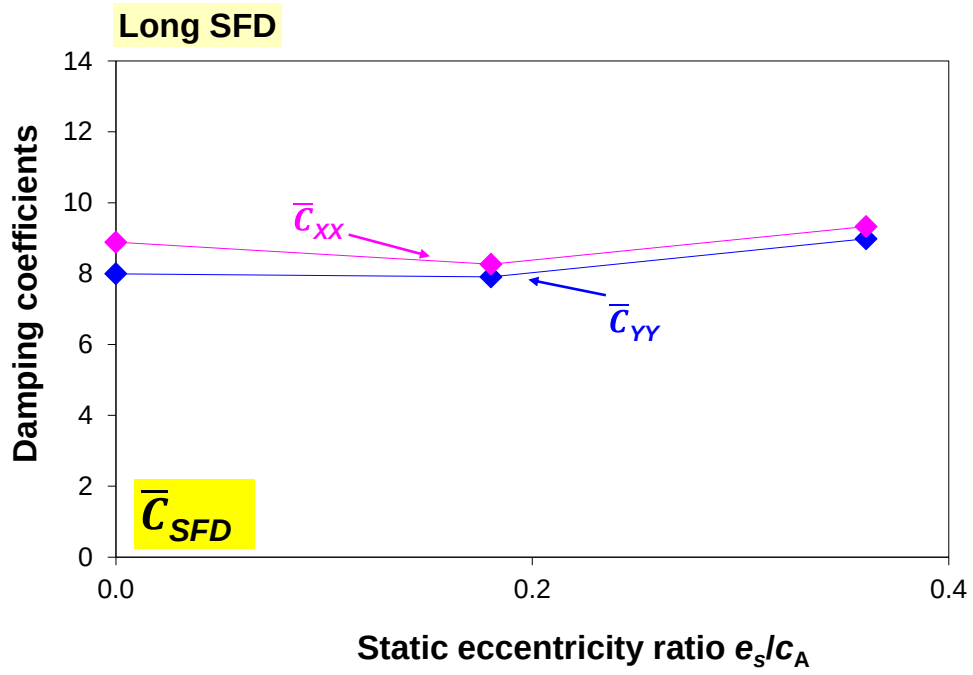

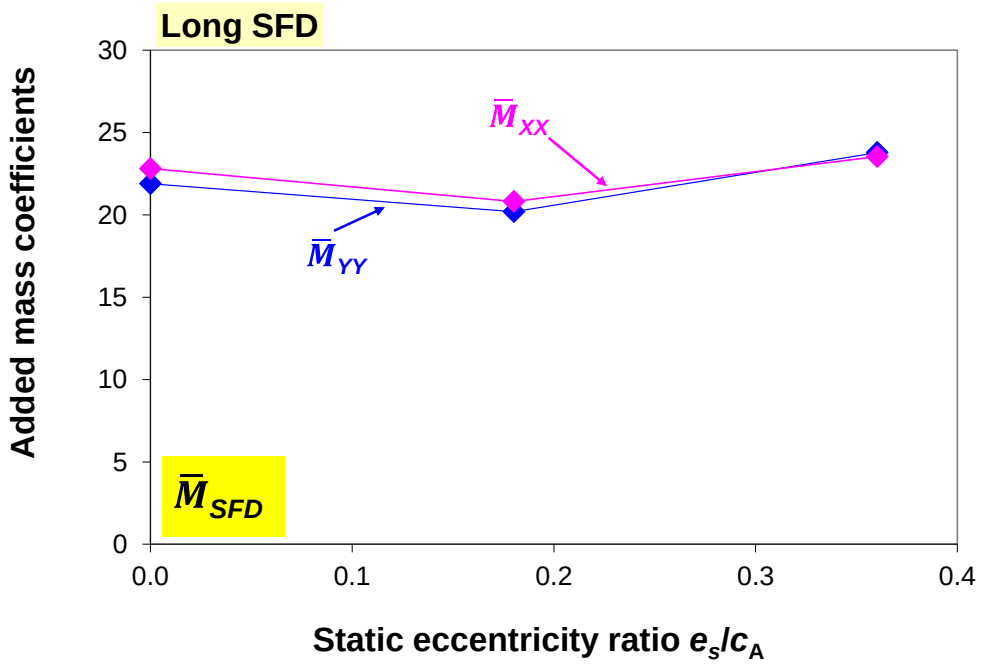

Figure 24. Long sealed ends damper. Direct damping, $(\bar{C}_{XX},\bar{C}_{YY})_{SFD}$, and added mass, $(\bar{M}_{XX}, \bar{M}_{YY})_{SFD}$,coefficients versus static eccentricity ratio (e_S/c_A). Test data obtained from circular orbits of amplitude r=0.054c_A

CHAPTER VIII

SAMPLE MEASUREMENTS OF DYNAMIC PRESSURE IN THE FILM LANDS AND GROOVE FOR TWO END SEALED SFDs

The aim is to measure the squeeze film dynamic pressures at the mid axial length of the film lands. Since the short and long dampers have different axial lengths, the sensors locations differ from one configuration to the other. Figure 25 shows the axial location of the dynamic pressure sensors for the two configurations. Thus, some holes will not contain a pressure sensor but a dummy steel probe. In both cases, the sensors are flush mounted, facing directly into the film land at its mid axial length.

For test configurations A and B, Figure 26 depicts a schematic view of the coordinate system and angle θ for location of the pressure and displacement sensors. At two angular locations (120^o apart), four pressure sensors record the top and bottom film land pressures. A pressure gage located at $\theta=0^o$ records the absolute level of the groove pressure (P_G). In the central groove, two pressure sensors (120° apart) record the dynamic pressures.

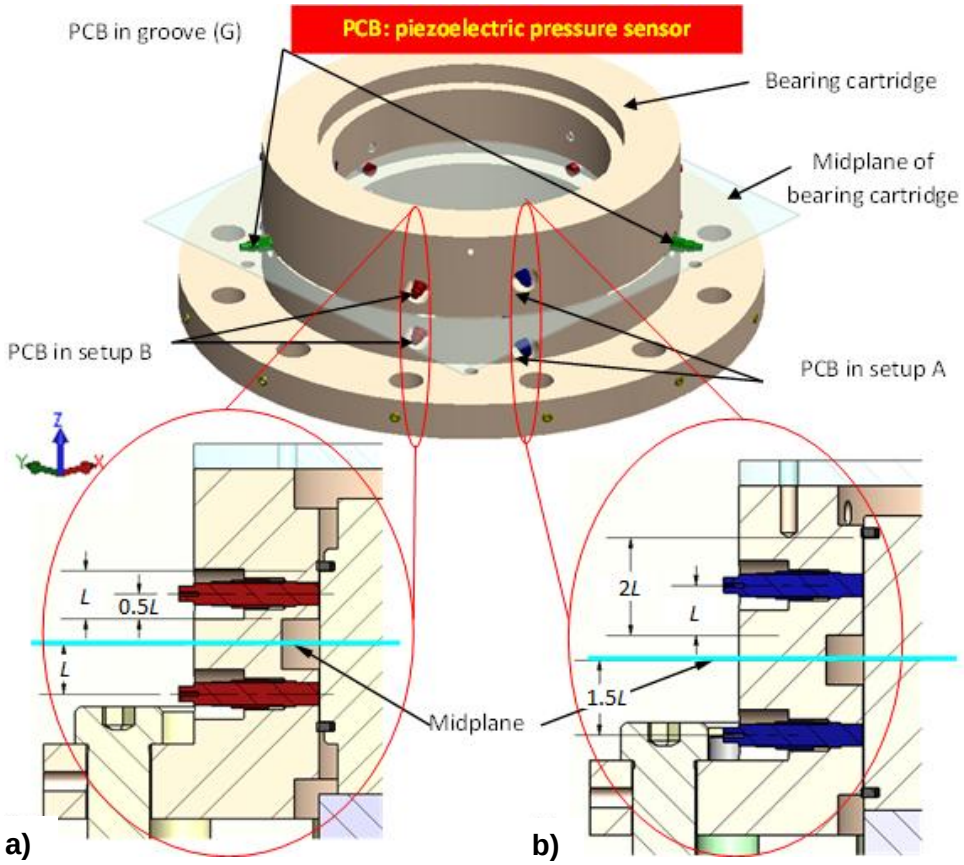

Figure 25. Disposition of pressure sensors in bearing cartridge. Cutaway views of bearing housing with pressure sensors placement for (a) short length damper: land lengths *L*, and (b) long damper: land lengths 2*L* [35]

Table 6. Installation of dynamic pressure sensors for short and long damper

Dynamic pressure sensors on BC		
Axial location	Long damper Angular location (θ)	Short length damper Angular location (θ)
Groove	165	165
Top	120	-150
Bottom	120	-150
Groove	285	285
Top	240	-30
Bottom	240	-30

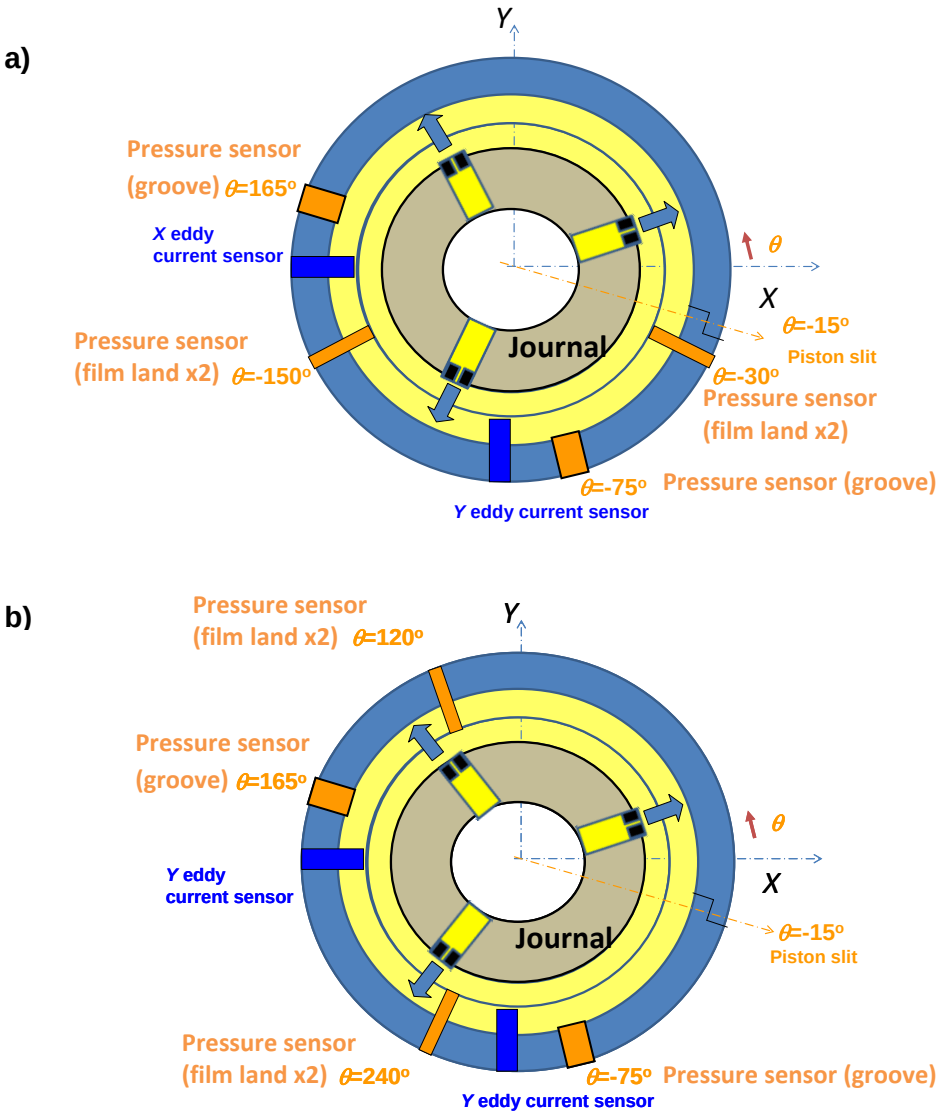

Figure 26. Schematic depiction of location of pressure sensors and eddy current sensors on bearing cartridge (a) long damper (b) short length damper

During dynamic load tests on the lubricated system, dynamic pressures are recorded in the film lands and in the central groove. The BC performs circular orbits of frequency ω and amplitude r about a static position e_S. The following graphs show typical recorded dynamic pressures obtained for four periods of whirl motion in the two sealed ends damper configurations.

Figure 27 illustrates the dynamic pressures in the film lands (top and bottom) at θ=120^o for two whirl frequencies (80 and 250 Hz). Figure 28 shows the dynamic pressures recorded in the central groove at θ=165^o and 285^o. The pressure signals are shifted an angle equal to the difference in angular position from one sensor to the other (θ_2–θ_1) =120^o. The horizontal axis denotes time in dimensionless form ($\tau=t\omega/2\pi$).

The magnitudes of the dynamic pressures are the same at the top and bottom film lands indicating that the journal has not tilted. However the pressures at the central groove show a dissimilarity, probably because of the near location of the groove sensor at θ=285^o to the piston ring slit opening (θ=345^o).

The dynamic pressure in the groove is similar in magnitude as the dynamic pressures in the film, indicating that the central groove does not separate the damper in two parallel film lands, but interacts with them.

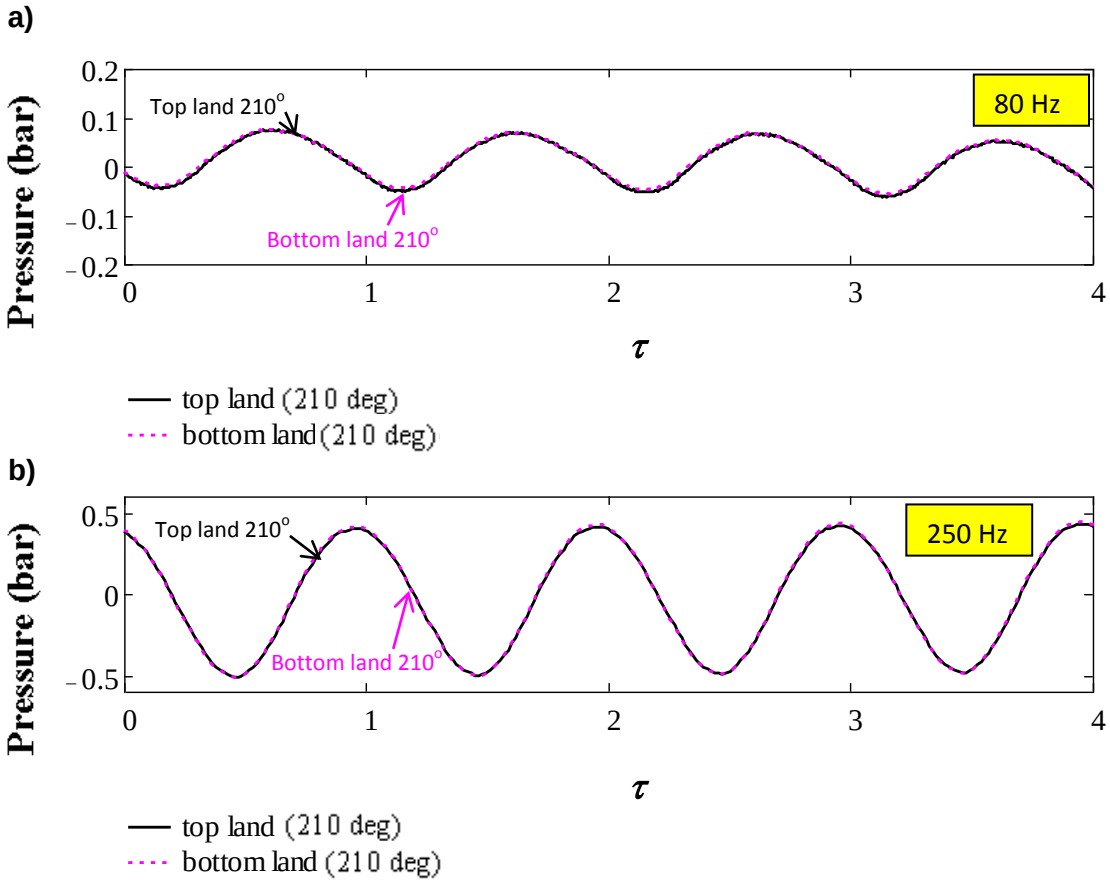

Figure 27. Short length sealed ends SFD. Dynamic pressures in film lands at θ =210° (top and bottom film lands). Whirl frequency (a) 80 Hz (b) 250 Hz. Centered BC (e_s=0), circular orbit r= 0.055c_B. Groove static pressure P_G =0.76 bar

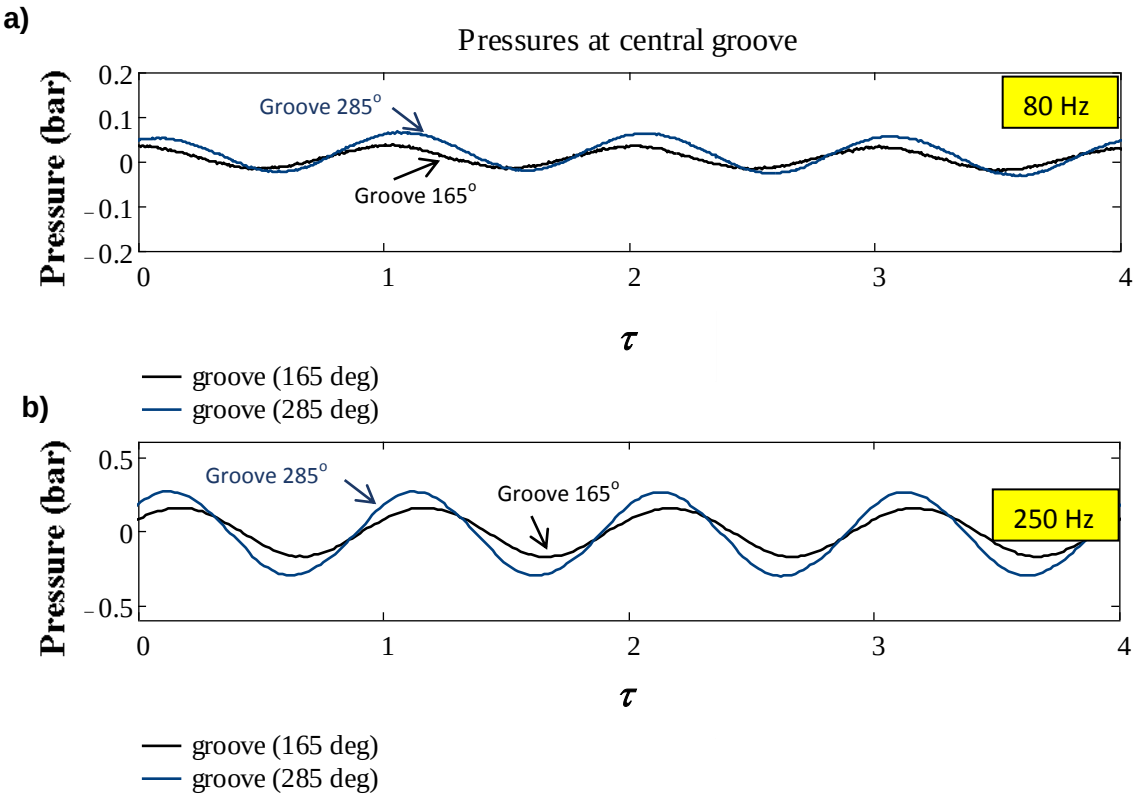

Figure 28. Short length sealed ends SFD. Dynamic pressures in central groove at θ =165° and 285° (top and bottom film lands). Whirl frequency (a) 80 Hz (b) 250 Hz. Centered BC (e_s=0), circular orbit r= 0.055c_B. Groove static pressure P_G =0.76 bar

For a test with the long damper Figure 29 illustrates the dynamic pressures in the film lands (top and bottom) at θ=240°, the dynamic pressures have slightly dissimilar amplitudes, indicating that the damper is not perfectly aligned with respect to the BC.

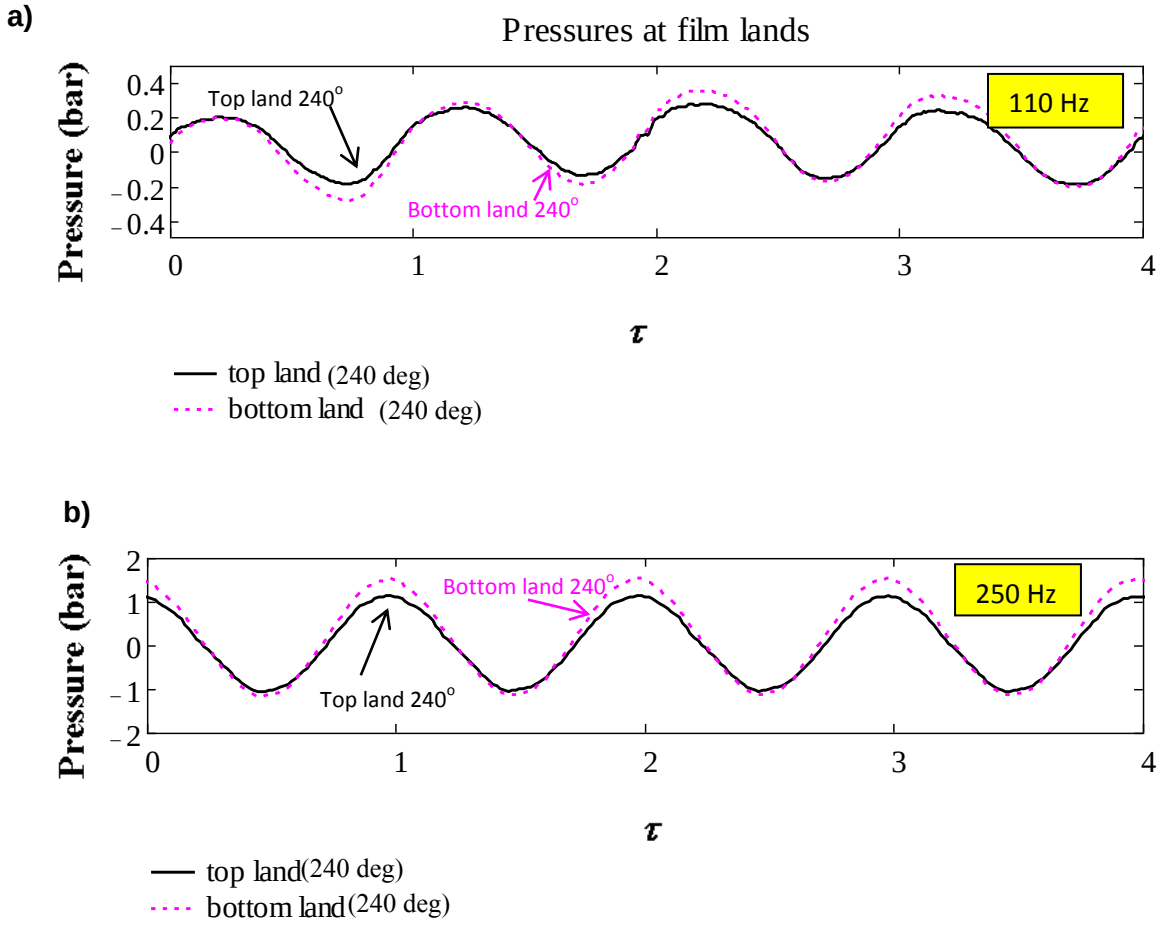

Figure 29. Long sealed ends SFD. Dynamic pressures in film lands at θ =240° (top and bottom film lands). Whirl frequency (a) 80 Hz (b) 250 Hz. Centered BC (e_s=0), circular orbit r= 0.055c_B. Groove static pressure P_G =4.69 bar

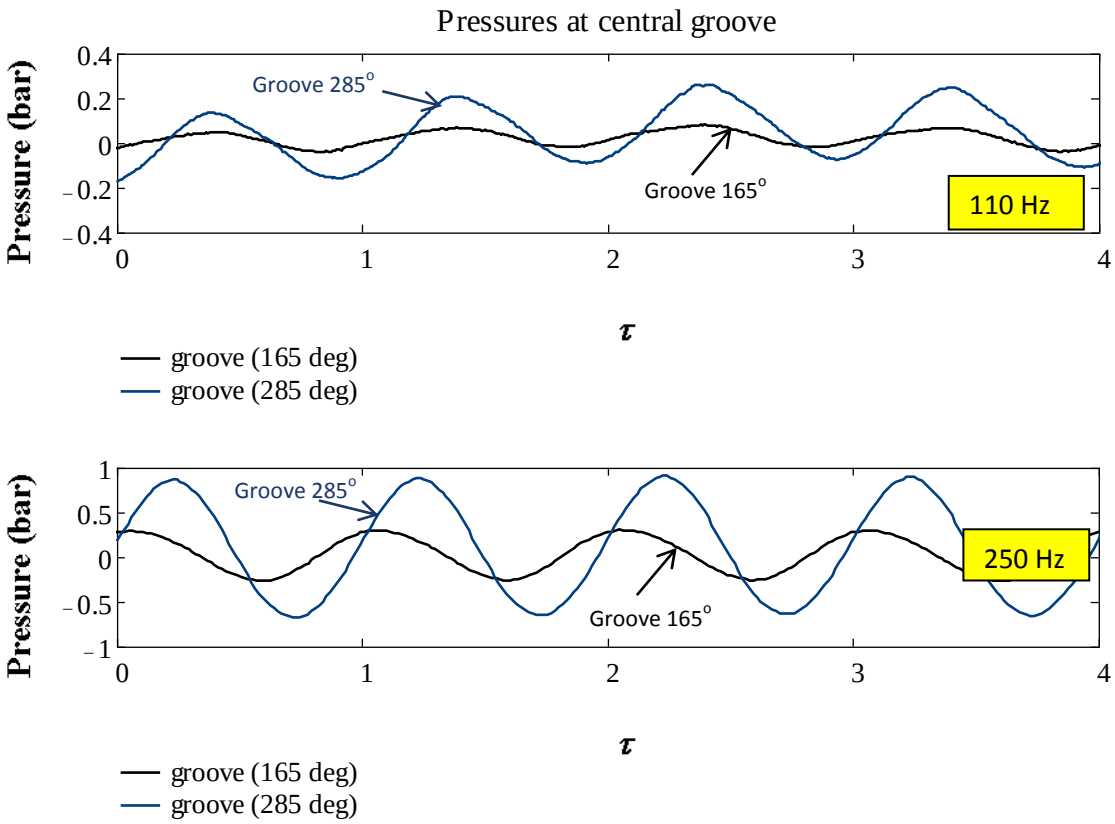

Figure 30. Short length sealed ends SFD. Dynamic pressures in central groove at θ =165° and 285° (top and bottom film lands). Whirl frequency (a) 80 Hz (b) 250 Hz. Centered BC (e_S=0), circular orbit r= 0.055c_B. Groove static pressure P_G =4.69 bar

Figures 31 and 32 show peak-peak pressures in the film lands and in the central groove versus whirl frequency for the short and long dampers, respectively. Note that the p-p pressures are larger for the long sealed SFD ~3.5 times larger, than for those in the short length damper. The dynamic film pressures appear to increase nearly linearly with whirl frequency.

Importantly enough, the dynamic pressure waveforms show that despite the large amplitude of the dynamic pressures, i.e., 3.5 bar peak-peak at 250 Hz for the long damper; there is no lubricant vapor or gas cavitation or air ingestion during the experiments. Recall that the pressure does not drop below ambient pressure since the supply pressure is 4.69 bar , thus avoiding the conditions for cavitation.

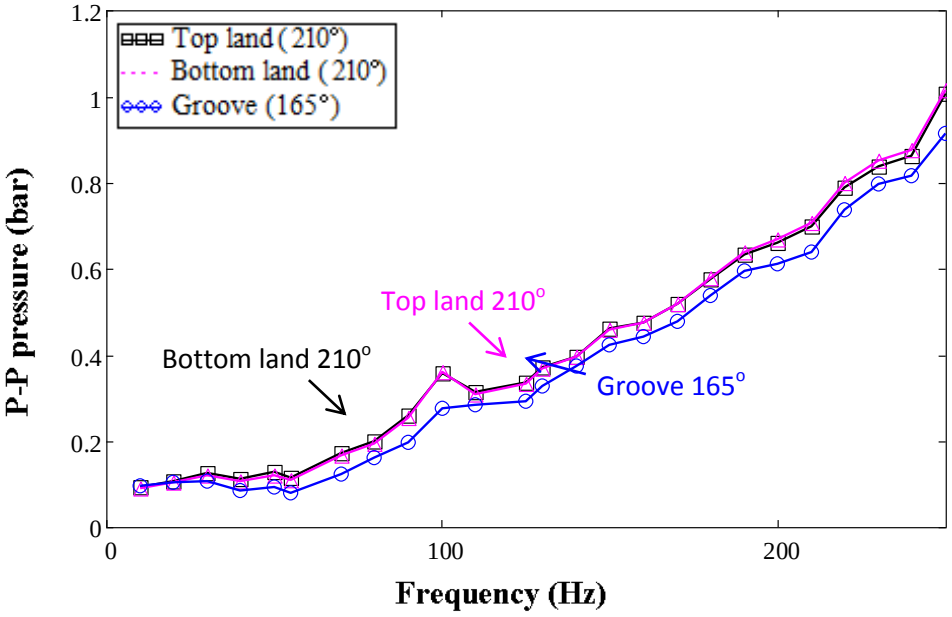

Figure 31. Short length sealed ends SFD. Peak-peak pressures in film lands and in central groove versus whirl frequency. Centered Bearing e_s=0, circular orbit r=0.1c_A. Groove pressure P_G = 0.72 bar

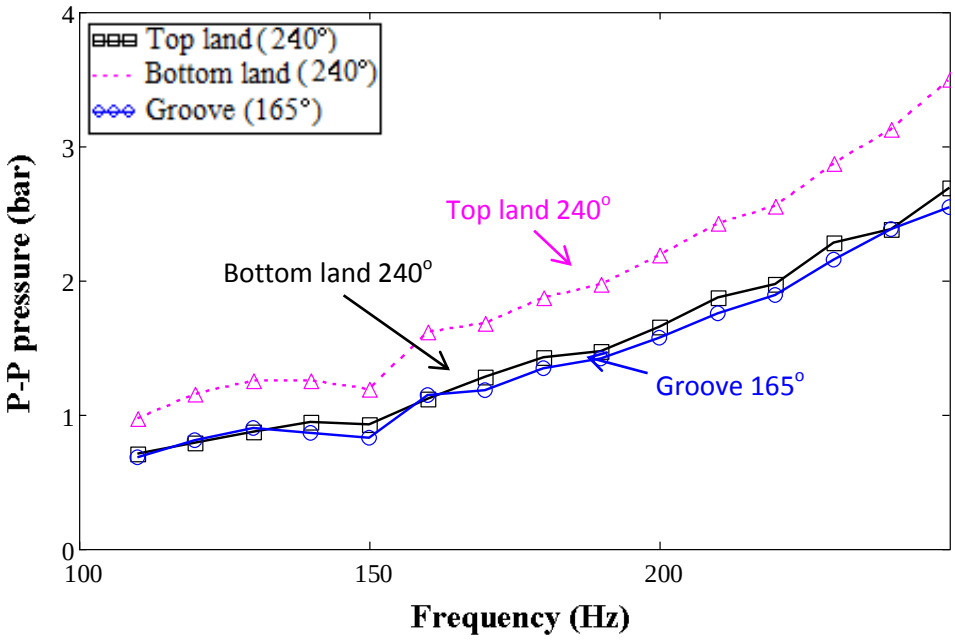

Figure 32. Long sealed ends SFD. Peak-peak pressures in film lands and in central groove versus whirl frequency. Centered bearing e_s=0, circular orbit r=0.1c_A. Groove pressure P_G = 4.69 bar

CHAPTER IX

COMPARISON OF SFD FORCE COEFFICIENTS: OPEN AND SEALED ENDS

Ref. [39] reports test data obtained from experiments performed on the same test rig for identical dampers but open ended.

The open ends configuration of the lubricated short length damper had a support stiffness (K_S) of 6.13 MN/m and a damped natural frequency f_n ~60 Hz. SFD force coefficients were determined from circular orbit tests of amplitude r=0.055c_B at the centered condition and for two static eccentricities e_S=0.29c_B and 0.44c_B. Note that the parameters were identified for frequencies ranging from 5 to 95 Hz since the system natural frequency (f_n) was lower.

The open ends long damper had structural support stiffness K_S=26.27 MN/m. Force coefficients were identified from circular orbits of amplitude r=0.090c_A, for a centered BC (e_S=0) and two static eccentricities e_S=0.23c_A and 0.37c_A. Force coefficients were identified for a frequency range from 110 to 210 Hz.

Table 7 lists the geometry, operating conditions, and fluid properties for test with the short and long open ends damper configurations reported in ref [39].

Table 7. Summary of SFD geometry, operating conditions and fluid properties for tests on the lubricated test system. Open ends SFDs

SFD geometry	**Long journal (A)**	**Short journal (B)**
Journal diameter	D=12.7cm	
Damper axial length	5L=63.5 mm	3L=38.1 mm
Radial land clearance	c_A=141.0 μm	c_B=137.9 μm
Central groove length	L_G=12.7mm	
Central groove depth	d_G=9.525 mm	
Operating conditions ISO VG2		
orbit amplitude (r)	0.090c_A	0.055c_B
Frequency range of identification	110-210 Hz	5-95 Hz
Static eccentricity (e_S)	0-0.36c_A	0-0.44c_B
Static stiffness (K_S)	26.27±0.15 MN/m	6.13±0.09MN/m
groove pressure (P_G)	0.68 bar (gage)	4.61 bar (gage)
Inlet flow rate (Q_{in})	4.92 LPM	4.92 LPM
Fluid properties		
Supply temperature (T_{in})	25 ^{o}C	
Viscosity at T_{in} (μ)	0.00296 Pa·s	
Density (ρ)	785 kg/m^3	

IX.1 Comparison of SFD force coefficients for the open ends and sealed ends short length dampers

Figure 33 shows the normalized (dimensionless) SFD damping and added mass force coefficients for the sealed ends and open ends short length dampers configurations versus static eccentricity ratio. The damping for the end sealed configuration is ~3.5 times larger than for the open ends damper at the centered condition (e_S=0). The added mass coefficients for the sealed damper are approximately twice as large as the coefficients for the end sealed configuration. The results prove the piston rings effectively increase the damping of the SFDs.

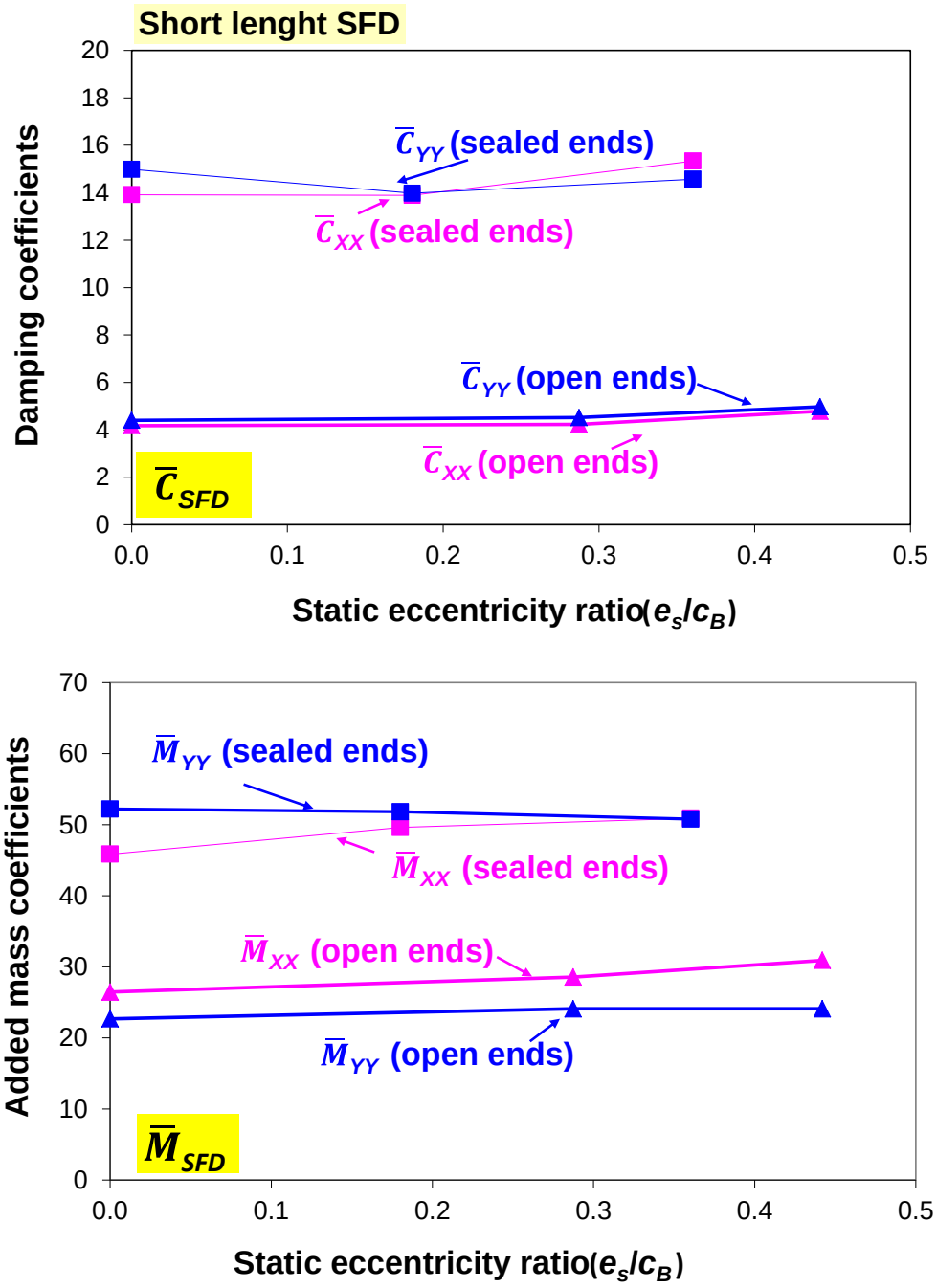

Figure 33. Short length open and sealed ends SFDs: Comparison of damping and inertia versus static eccentricity. Orbit radius r= 0.055c_B. Data for open ends SFD from Ref. [39]

IX.2 Comparison of SFD force coefficients from long damper open and sealed ends configurations

Figure 34 shows an increase in the damping coefficients from the open ends to the end sealed configuration, which is a direct effect of the piston rings installation. At the centered position direct damping coefficients $(\bar{C}_{XX}, \bar{C}_{YY})_{SFD}$ for the sealed condition are ~2.7 times larger than coefficients for the open ends. The added mass coefficients $(\bar{M}_{XX}, \bar{M}_{YY})_{SFD}$ for the sealed ends configuration are ~2.6 times larger than for the open ends SFD, i.e., a consequence of the lesser axial pressure gradient due to the end seal [40] .

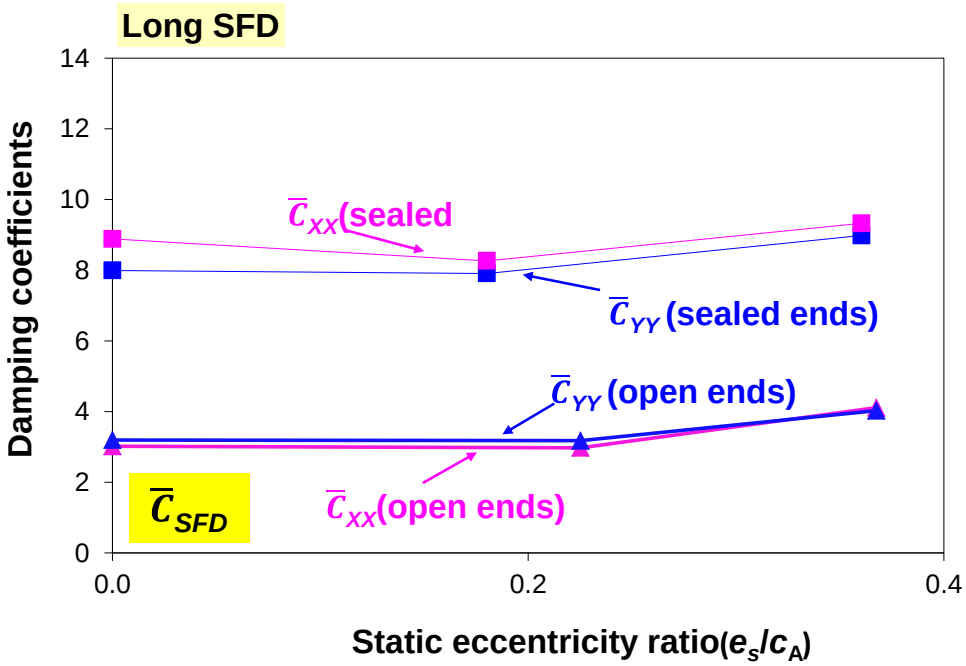

Figure 34. Long open and sealed ends SFDs: Comparison of damping and inertia versus static eccentricity. Orbit radius $r = 0.090c_A$ for the open ends and $r = 0.054c_A$ for the sealed ends. Data for open ends SFD from Ref. [39]

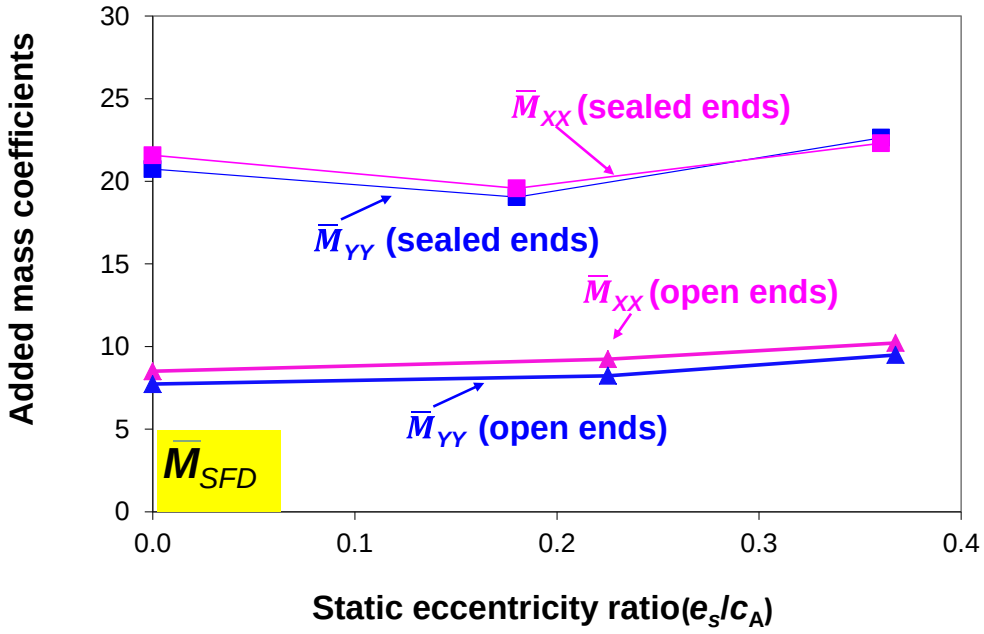

Figure 34. Continued

CHAPTER X

COMPARISON OF TEST COEFFICIENTS WITH PREDICTIONS OBTAINED FROM A COMPUTATIONAL ANALYSIS

The experimentally determined force coefficients from tests with the two sealed ends SFDs, presented in Chapter VII, are compared to predictions from a computational tool developed by San Andrés [15].

The novel computational model uses the finite element method (FEM) to solve the modified Reynolds equation governing the fluid flow in the damper lands and groove [10]

$$\frac{\partial}{\partial x}\left(h^3\frac{\partial P}{\partial x}\right)+\frac{\partial}{\partial z}\left(h^3\frac{\partial P}{\partial z}\right)=12\,\mu\frac{\partial h}{\partial t}+\rho h^2\,\frac{\partial^2 h}{\partial t^2} \tag{26}$$

where ρ and μ are the lubricant density and viscosity, respectively, and P is the pressure and h is the film thickness

$$h_{(\Theta,z,t)}=c_{(z)}+e_{X_{(t)}}\cos(\Theta)+e_{Y_{(t)}}\sin(\Theta) \tag{27}$$

where $c_{(z)}$ is a step-wise clearance distribution along the axial direction and (e_X ,e_Y) are the components of the journal center eccentricity.

The modified Reynolds equation includes temporal fluid inertia effects and is valid for small amplitudes of journal motions about an equilibrium position.

The code can solve open ended as well as sealed SFD configurations. In addition the code can model central feed grooves and feed holes

To predict the SFD force coefficients the code needs an effective groove depth (d_η) that differs from the physical groove depth (d_G). Recall that the dynamic pressures measured in the groove are significant when compared to those in the film lands as demonstrated in Chapter VIII. Hence, the contribution of the groove to the SFD forced performance cannot be disregarded. The following subsections show that the effective groove depth is just a few times the clearance even when the physical groove is ~75c.

In the predictive code, an end seal is modeled as a local flow/per unit circumferential length that is proportional to the pressure drop, i.e.,

$$q\left[\frac{\mathrm{m}^3}{\mathrm{s\,m}}\right]=\frac{Q}{\pi D}=C_{SEAL}\left(P_{z=L_E}-P_a\right) \tag{28}$$

where C_{SEAL} has physical units of [(m^2/s)/bar] and L_E is the exit plane of the damper land. The relationship between the seal overall conductance (C_s), and the seal coefficient used in the code is

$$C_{SEAL}=\frac{C_S}{\pi D} \tag{29}$$

The code is written in FORTRAN with a graphical use interface in MS Excel®. The user inputs the SFD geometry, the end seal coefficient (C_{SEAL}), the operating conditions, and the fluid properties and the code delivers the linearized SFD force coefficients (K, C, M)$_{\mathrm{SFD}}$. Table 8 lists the user inputs for prediction of the SFD force coefficients for the long and short length damper configurations.

Table 8. Geometry, oil properties and operating conditions for prediction of SFD force coefficients

SFD geometry	**Long journal (A)**	**Short journal (B)**
Journal diameter	D=12.7cm	
Damper axial length (groove + 2 lands)	5L=63.5 mm	3L=38.1 mm
Radial land clearance	c_A=141.0 μm	c_B=137.9 μm
Effective groove depth (d_η)	2c_A	2.5c_B
Central groove axial length	L_G=12.7mm	
Central groove depth	d_G=9.525 mm	
Seal coefficient (C_{SEAL})	5.83 x 10^{-5} (m^2/s)/bar	6.25 x 10^{-6}(m^2/s)/bar
Operating conditions		
Ambient pressure (P_a)	0 (gage)	
Static eccentricity (e_S)	0-0.36c_A	0-0.37c_B
Groove pressure (P_G)	0.68 bar (gage)	4.61 bar (gage)
Radial feed holes (x3)	120^o apart	

Table 8. Continued

Fluid properties	
Oil cavitation pressure (P_{cav})	-1.01 bar
Supply temperature (T_{in})	25 ^{o}C
Viscosity at T_{in} (μ)	0.00296 Pa·s
Density (ρ)	785 kg/m^3

X.1 Comparisons between experimental and predicted force coefficients for the short length damper

For the short length damper operating with small amplitude motions about the centered position, Figure 35 shows computational predictions of direct damping ($\bar{C}_{XX}$, $\bar{C}_{YY}$)$_{\mathrm{SFD}}$ and added mass ($\bar{M}_{XX}$, $\bar{M}_{YY}$)$_{\mathrm{SFD}}$ coefficients versus effective groove depth plus clearance. The figure also includes test data derived from CCOs tests with amplitude r=0.055c_B as conducted with the short length damper. Experimental data at the centered position serves to determine the effective groove depth to be used in the predictive code. The effective groove depth is 2.5c for the short length damper.

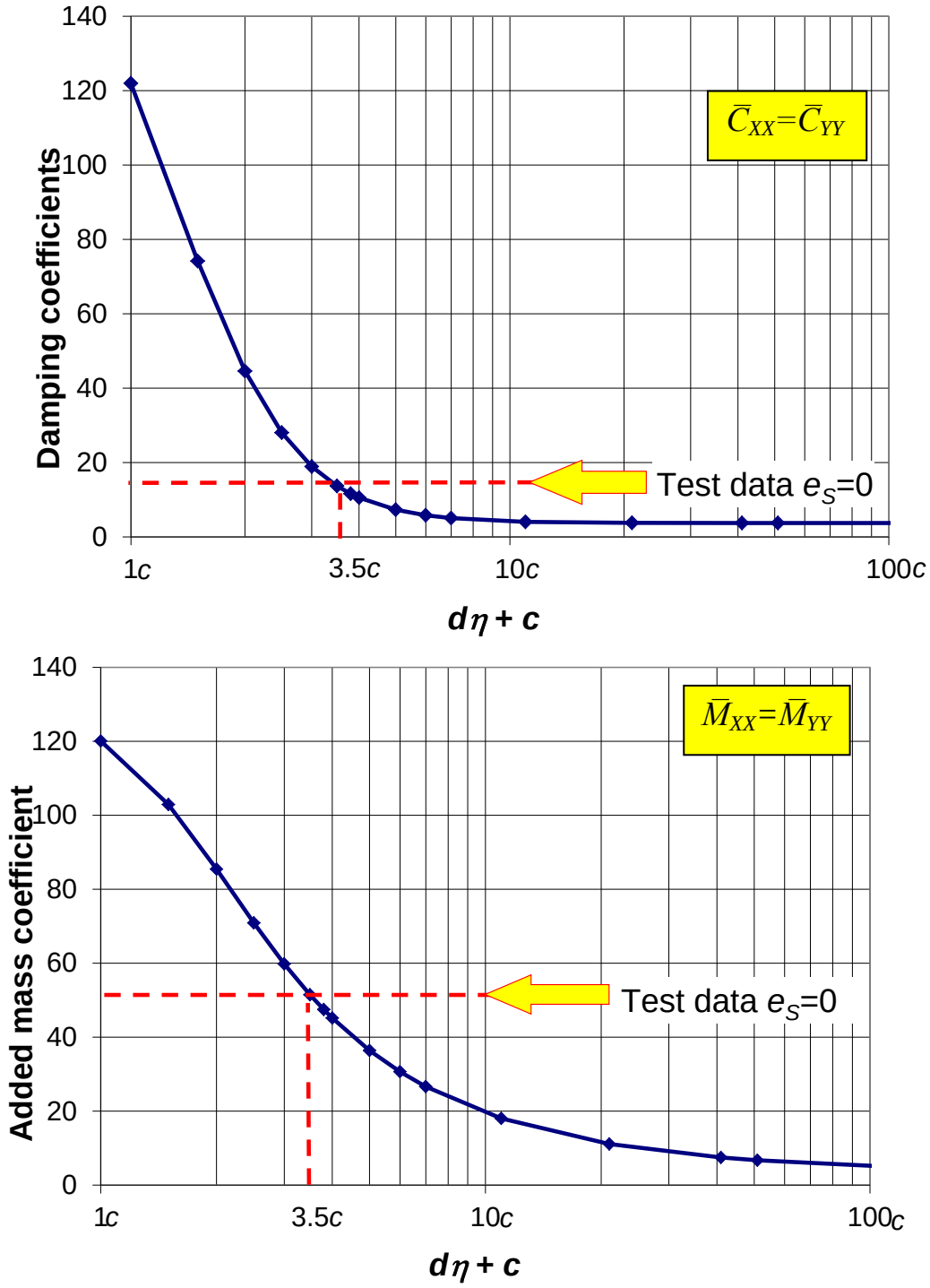

Figure 35. Sealed ends short SFD: Predicted SFD damping ($\bar{C}_{XX}$,$\bar{C}_{YY}$)SFD and added mass ($\bar{M}_{XX}$,$\bar{M}_{YY}$)SFD coefficients versus effective groove depth plus clearance. Centered condition (e_S=0). Test data overlaid with predictions to estimate effective groove depth (d_η)

The effective groove depth is used as an input to the computational code to predict the SFD force coefficients over a range of static eccentricity ratios.

For the short length damper, Figure 36 shows the experimentally identified damping and fluid inertia coefficients and predictions versus static eccentricity. The damping coefficients agree well with the experimental values. The predictions and the experimental data show damping coefficients increasing with the static eccentricity while the added mass coefficients are nearly constant. Also, predicted cross-coupled force coefficients are negligible for the operation considered, i.e., small amplitude journal motions about a static position. Note that with the information derived from only one experiment, the code is capable of predicting the SFD forced response at different static eccentricities with remarkable agreement.

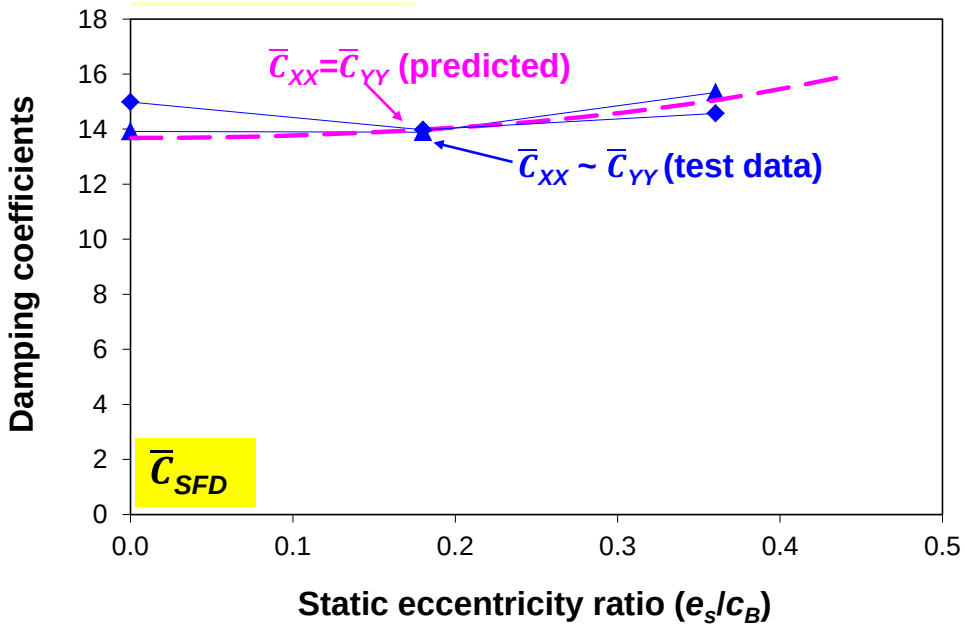

Figure 36. Short length sealed ends SFD: Normalized predicted and experimental damping ($\bar{C}_{XX}$,$\bar{C}_{YY}$) and added mass ($\bar{M}_{XX}$,$\bar{M}_{YY}$) coefficients versus static eccentricity. Effective groove depth d_η=2.5c

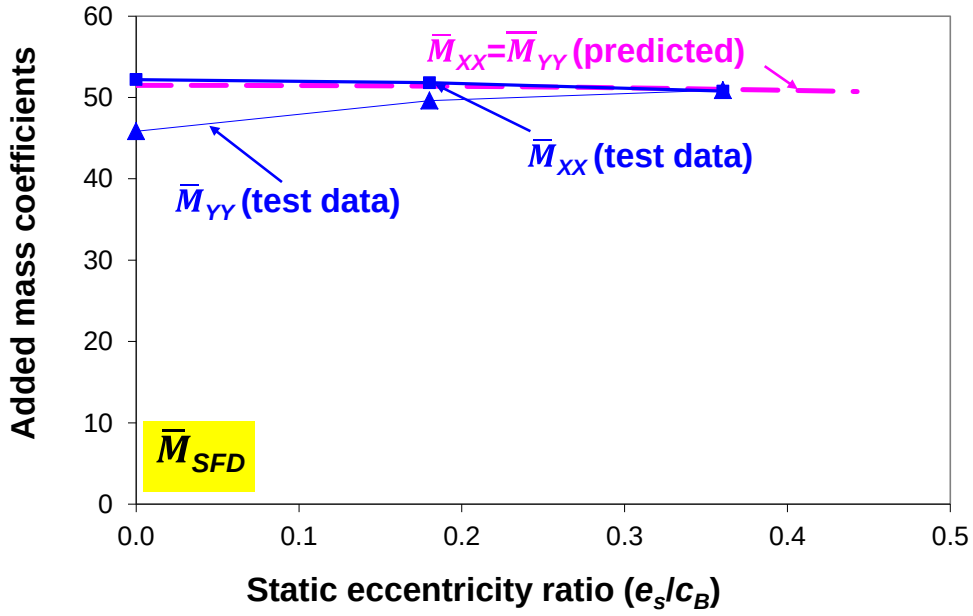

Figure 36. Continued

X.2 Comparisons between experimental and predicted force coefficients for the long damper

For the sealed ends long damper executing small amplitudes of motion about the centered condition, Figure 37 shows predictions of the SFD direct damping and added mass coefficients versus the effective groove depth plus clearance. In the figure, a horizontal line denotes the coefficients identified from tests at the centered condition. The effective groove depth ($d_\eta = 2c$) is obtained at the intersection of the predictions and the identified coefficients.

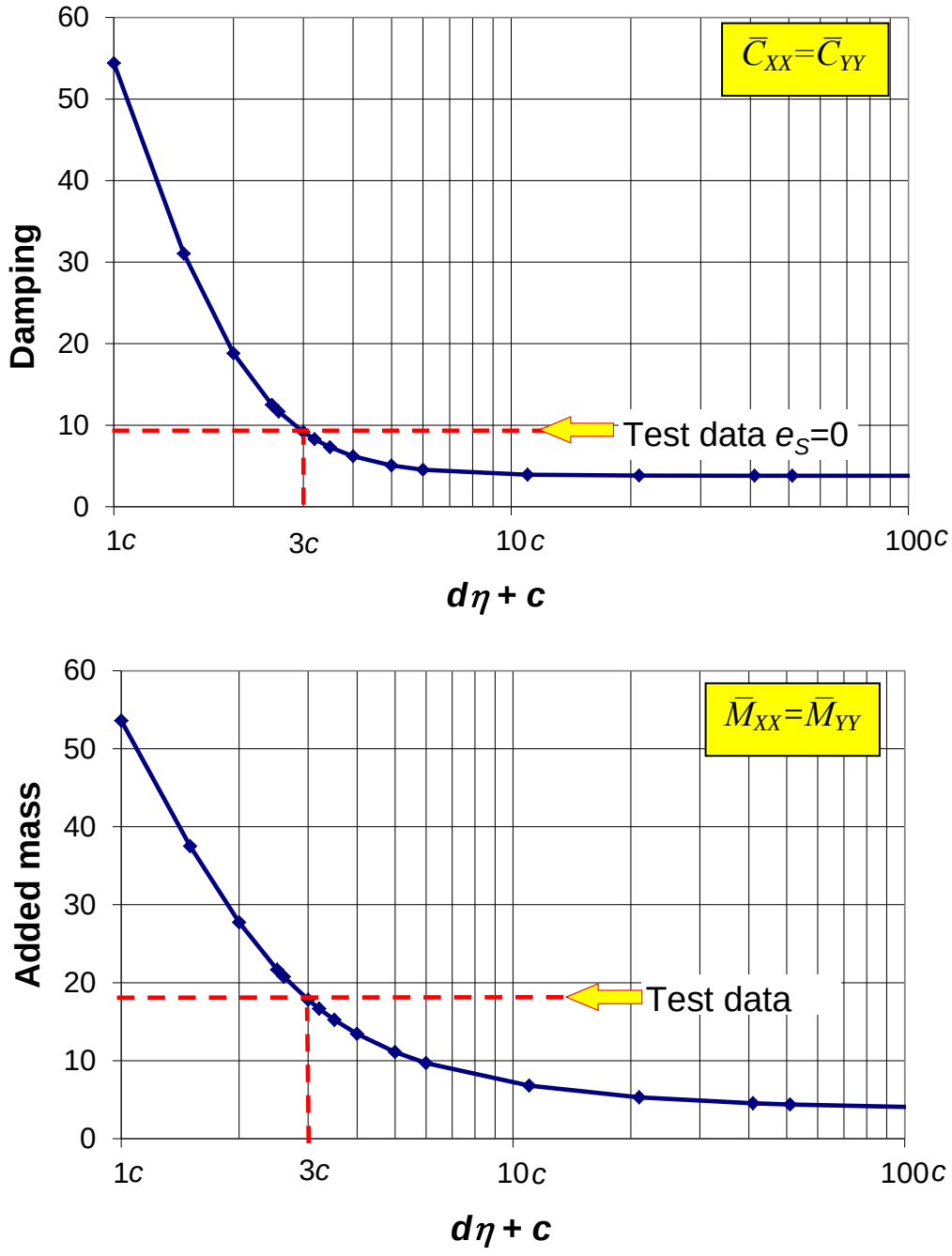

Figure 37. Sealed ends long SFD: predicted SFD damping ($\bar{C}_{XX}$, $\bar{C}_{YY}$)SFD and added mass ($\bar{M}_{XX}$,$\bar{M}_{YY}$)SFD coefficients versus effective groove depth plus clearance. Centered condition (e_S=0). Test data overlaid with predictions to estimate effective groove depth (d_η)

For tests on the long damper, Figure 38 shows test data and predictions of the damping ($\bar{C}_{XX}$, $\bar{C}_{YY}$) and added mass coefficients ($\bar{M}_{XX}$, $\bar{M}_{YY}$). The predicted damping increases with the static eccentricity and corresponds well with the experimental data. However, the added mass coefficients are under predicted by ~25%. The predicted mass is constant with static eccentricity while the test identified parameters seem to decrease and then increase with static eccentricity.

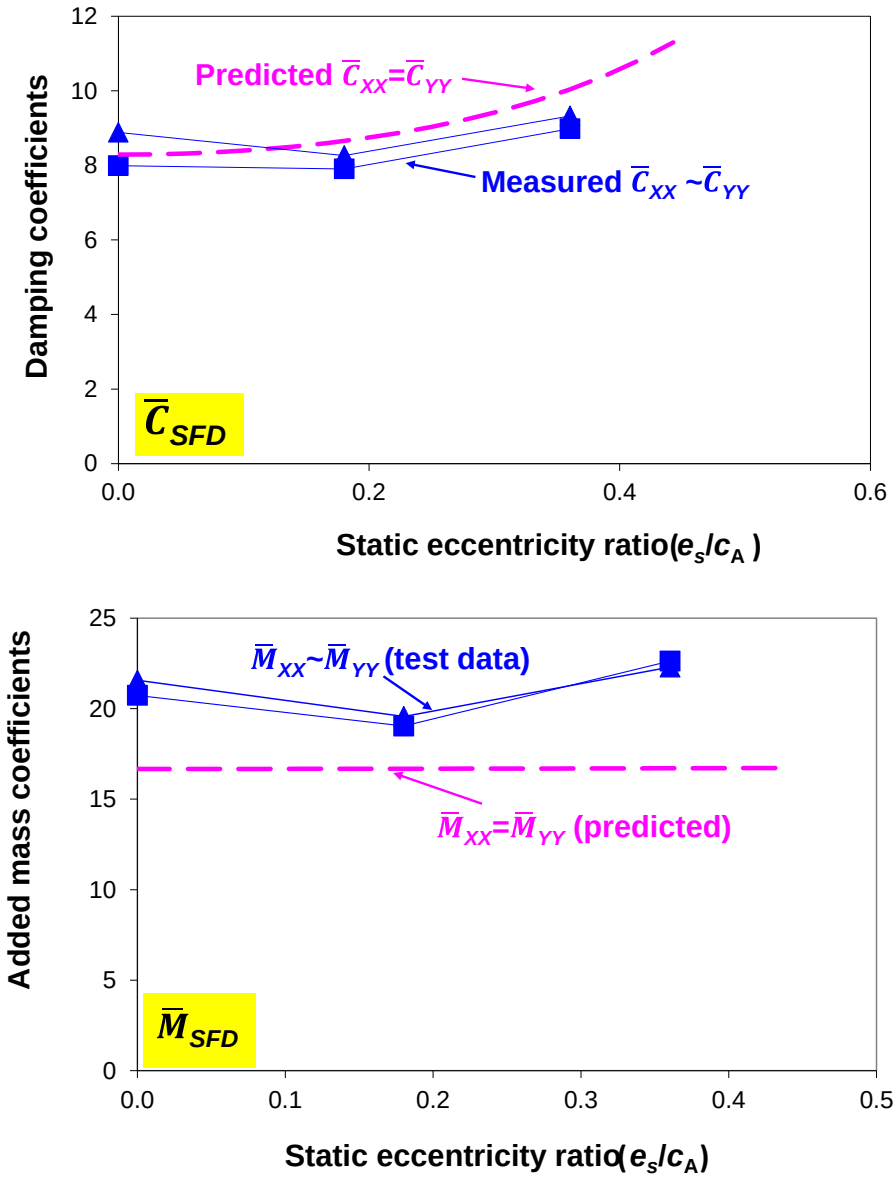

Figure 38. Long sealed ends SFD: Predicted and experimental damping and inertia force coefficients versus static eccentricity. Effective groove depth d_η=2c

The squeeze film Reynolds number $Re_s = \rho\omega c^2/\mu$ represents the ratio of inertial to viscous film forces. In SFD_s, Re_s>12 defines the threshold where fluid inertia forces exceed viscous forces [10, 47]. Recall that at the central groove the clearance is larger ($d_\eta + c$=3.5c). A simple calculation demonstrates that in the central groove significant fluid inertia effects (direct added mass coefficients) are induced. i.e., for the short damper operating at ω=1570.8 rad/s (250 Hz), the squeeze film Reynolds number in the film lands is Re_s=7.9(<12) while in the central groove is Re_s= 97.0(>12).

CHAPTER XI

CONCLUSIONS

For two centrally grooved sealed ends dampers, the IVFM identifies the SFD force coefficients from circular orbit tests at the centered position and at various static eccentricities. The thesis presents comparisons of SFD force coefficients for the sealed damper to a simplified open ends SFD model that does not account for the central groove to test results from the same damper but open ended, and also to predictions from a FEM based solution. The main conclusions of this work are:

XI.1 Sealed ends short length damper (L_B=127 mm, c_B=137.9 μm)

For the short length damper, SFD force coefficients derived from circular orbits of amplitude r=0.055c_B for static eccentricity (e_S) varying from 0 to 0.36c_B over a frequency range 50 - 250 Hz, show:

- The damping and added mass coefficients remain nearly constant with static eccentricity.
- The experimental added mass coefficients are ~50 times and the damping coefficients are ~15 times larger than the corresponding coefficients derived from a simplified model (no groove) for an open ends damper.
- When compared to results from the same SFD but open ended, the added mass is ~2 times larger for the sealed ends long damper. The sealed ends damper has ~ 3.8 times more damping than the open ends damper.
- Predictions of the SFD force coefficients using a novel computational model that accounts for the central groove and the feed system are in excellent agreement with experimental results from the short length damper when using an effective groove depth d_η=2.5c.

XI.2 Sealed ends long damper (L_A=254 mm, c_A=141.0 μm)

For the long damper, SFD force coefficients derived from circular orbits of amplitude r=0.054c_B for static eccentricity (e_S) varying from 0 to 0.37c_A, and excitation frequencies ranging from 110 to 250Hz, show:

- The added mass coefficients first increase and then decrease with static eccentricity. The damping coefficients increase mildly with static eccentricity.
- The damping coefficients are ~8 times larger and added masses ~23 times larger than predicted by a simplified model for an open ends damper that disregards the central groove, demonstrating the influence of both the seals and the central groove in the SFD forced performance.
- Comparison to results from an open ends configuration evidence the seals increase the damping coefficients by ~2.8 times. The added mass coefficients are ~3.1 times larger for the sealed ends configuration when compared to the open ends.
- The experimental damping coefficients agree well with predictions. However, the added mass coefficients are under predicted by ~25%.

XI.3 Both dampers

- In general the SFDs do not generate stiffness coefficients, except for the long damper operating at the largest static eccentricity (e_S=0.36c_A).
- The SFD cross-coupled force coefficients are at least an order of magnitude smaller than the direct coefficients. The low cross-coupled coefficients demonstrate that the test rig operates without air ingestion or cavitation (gas or vapor).
- Comparisons of the test results with classical lubrication theory evidence large added mass coefficients and damping coefficients, demonstrating that the central groove has a large influence on the SFD forced performance.

- The sealed ends damper configurations present more damping and added mass coefficients than an open ends damper; a direct effect of the lesser axial pressure gradient caused by the end seal
- The dynamic pressures in the central groove are as large as those in the film lands, thus demonstrating the significant influence of the central groove on the SFD forced performance.
- Comparisons to experimental results from the same test rig with open ends configuration demonstrate that the end seals effectively seal the damper and increase the damping in the system. Piston ring seals help to prevent air ingestion and effectively increase the direct damping.

REFERENCES

[1] Zeidan, F. Y., San Andrés, L., and Vance, J. M., 1996, "Design and Application of Squeeze Film Dampers in Rotating Machinery," *Proceedings of the 25th Turbomachinery Symposium*, Turbo-machinery Laboratory, Texas A&M University, College Station,TX, pp. 169–188.

[2] San Andrés, L. A., and Vance, J. M., 1987, "Experimental Measurement of the Dynamic Pressure Distribution in a Squeeze Film Damper Executing Circular Centered Orbits " ASLE Trans., **30**(3), pp. 373-383.

[3] Ramli, M. D., Roberts, J. B., Ellis, J., 1987, "The Determination of Squeeze Film Dynamic Coefficients from Experimental Transient Data," ASME J. Tribol., **109**(1), pp. 155-163.

[4] San Andrés, L., 1992, "Analysis of Short Squeeze Film Dampers With a Central Groove," ASME J. Tribol., **114**(4), pp. 659-664.

[5] Arauz, G., and San Andrés, L., 1993, " Experimental Pressures and Film Forces in a Squeeze Film Damper," ASME J. Tribol, **115**(1), pp. 134-140.

[6] Arauz, G., and San Andrés, L., 1994, "Effect of a Circumferential Feeding Groove on the Dynamic Force Response of a Short Squeeze Film Damper," ASME J. Tribol, **116**(2), pp. 369-377.

[7] Arauz, G. L., and San Andrés, L., 1997, "Experimental Force Response of a Grooved Squeeze Film Damper," Tribol. Int., **31**(5), pp. 265-270.

[8] Diaz, S., and San Andrés, L., 2001, "Air Entrainment Versus Lubricant Vaporization in Squeeze Film Dampers: An Experimental Assessment of Their Fundamental Differences," ASME J. Eng. Gas Turbines Power, **123**(4), pp. 871-877.

[9] Delgado, A., and San Andrés, L., 2010, "Identification of Force Coefficients in a Squeeze Film Damper With a Mechanical Seal: Large Contact Force," ASME J. Tribol., **132**(3), p. 032201.

[10] San Andrés, L., 2010, "Squeeze Film Dampers (SFDs)," Modern Lubrication Theory, Notes 13, Texas A&M University Digital Libraries, https://repository.tamu.edu/handle/1969.1/93197. 01/02/2011

[11] Channasandra, N., 2011, Manager, Engine Dynamics & Loads at Pratt & Whitney UTC, private communication.

[12] Adiletta, G., and Della Pietra, L., 2002, "The Squeeze Film Damper over Four Decades of Investigations. Part II: Rotordynamic Analyses with Rigid and Flexible Rotors," Shock Vib. Dig., **34**(2), pp. 97-126

[13] Adiletta, G., and Della Pietra, L., 2006, "Experimental Study of a Squeeze Film Damper With Eccentric Circular Orbits," ASME J. Tribol., **128**(2), pp. 365-377.

[14] Pan, C. H. T., and Tonessen, J., 1978, "Eccentric Operation of Squeeze-Film Damper," J. Lubr. Tech., **2**(100), pp. 369-377.

[15] San Andrés, L., 2010, "PW_SFD_2010," SFD Predictive Code Developed for Pratt & Whitney Engines, MEEN Dept., Texas A&M University.

[16] Della Pietra, L., Adiletta, G., 2002, "The Squeeze Film Damper over Four Decades of Investigations. Part I: Characteristics and Operating Features," Shock Vib. Dig, **34**(1), pp. 3-26.

[17] Cooper, S., 1963, "Preliminary Investigation of Oil Films for Control of Vibration," Proc. Lubrication and Wear Convention, Inst. Mech. Eng., pp. 305-315.

[18] San Andrés, L., and Vance, J. M., 1987, "Effects of Fluid Inertia on Finite-Length Squeeze Film Dampers," ASLE Trans., **30**(3), pp. 384-393.

[19] Qingchang, T., Ying, C., Lyjiang, W., 1997, "Effect of a Circumferential Feeding Groove on Fluid Force in Short Squeeze Film Dampers," Tribol. Int., **30**(6), pp. 409-416.

[20] Arauz, G. L., and San Andrés, L., 1996, "Experimental Study on the Effect of a Circumferential Feeding Groove on the Dynamic Force Response of a Sealed Squeeze Film Damper," ASME J. Tribol., **118**(4), pp. 900-905.

[21] Ramli, M. D., Roberts, J. B., and Ellis, J., 1996, "Force Coefficients for a Centrally Grooved Short Squeeze Film Damper," ASME J. Tribol., **118**(3), pp. 608-616.

[22] Lund, J. W., Myllerup, C. M., and Hartmann, H., 2003, "Inertia Effects in Squeeze-Film Damper Bearings Generated by Circumferential Oil Supply Groove," J. Vib. Acoust., **125**(4), pp. 495-499.

[23] Kim, K. J., and W., L. C., 2005, "Dynamic Characteristics of Sealed Squeeze Film Damper With a Central Feeding Groove," ASME J. Tribol., **127**(1), pp. 103-111.

[24] Levesley, M. C., and Holmes, R., 1996, "The Effect of Oil Supply and Sealing Arrangements on the Performance of Squeeze-Film Dampers: An Experimental Study," J. Eng. Tribol., **210**(J4), pp. 221-232.

[25] Diaz, S. E., and San Andrés, L., 1999, "Reduction of the Dynamic Load Capacity in a Squeeze Film Damper Operating with a Bubbly Lubricant," ASME J. Eng. Gas Turbines Power, **121**, pp. 703-709.

[26] Diaz, S. E., and San Andrés, L., 1998, "Measurements of Pressure in a Squeeze Film Damper with an Air/Oil Bubbly Mixture," STLE Tribol. Trans., **41**, pp. 282-288.

[27] Diaz, S., and San Andrés, L., 2001, "A Model for Squeeze Film Dampers Operating with Air Entrainment and Validation with Experiments," ASME J. Tribol, **123**(1), pp. 125-133.

[28] San Andrés, L., and Delgado, A., 2008, "Squeeze Film Damper With a Mechanical End Seal: Experimental Force Coefficients Derived From Circular Centered Orbits," ASME J. Eng. Gas Turbines Power, **130**(4), pp. 505-508.

[29] San Andrés, L., and Delgado, A., 2007, "Identification of Force Coefficients in a Squeeze Film Damper With a Mechanical End Seal. Part I: Unidirectional Load Tests," ASME J. Eng. Gas Turbines Power, **129**(3), pp. 858-864.

[30] Delgado, A., and San Andrés, L., 2009, "Nonlinear Identification of Mechanical Parameters in a Squeeze Film Damper With Integral Mechanical Seal," ASME J. Eng. Gas Turbines Power, **131**(4), p. 042504.

[31] Delgado, A., 2008, "A Linear Fluid Inertia Model For Improved Prediction Of Force Coefficients In Grooved Squeeze Film Dampers And Grooved Oil Seal Rings," PhD Dissertation, Texas A&M University, College Station, TX.

[32] Delgado, A., and San Andrés, L., 2010, "A Model for Improved Prediction of Force Coefficients in Grooved Squeeze Film Dampers and Oil Seal Rings," ASME J. Tribol., **132**(3), p. 032202.

[33] Gehannin, J., and Arghir, M., 2010, "Complete Squeeze-film Damper Analysis Based on the “Bulk Flow” Equations," Tribol. Trans., **53**(1), pp. 84-96.

[34] Defaye, C., Arghir, M., and Bonneau, O., 2006, "Experimental Study of the Radial and Tangential Forces in a Whirling Squeeze Film Damper," Tribol. Trans., **49**, pp. 271-278.

[35] San Andrés, L., 2010, "Description of P&W SFD Test Rig (Construction and Operation) and Identification of Test System Parameters (Dry and Lubricated)," Annual Report (Y II) to Pratt & Whitney UTC, January.

[36] San Andrés, L., 2008, "P&W SFD Test Rig: Design and Statement of Work for 2009-2010," Design Report to Pratt & Whitney UTC, December.

[37] San Andrés, L., 2010, Monthly Progress Report #21 to Pratt & Whitney UTC,Technical Report No. 21, October 2010.

[38] Delgado, A., 2008, "VTR-SFD CCO code," LabVIEW Virtual Instrument developed for TRC Vertical SFD test rig.

[39] Seshagiri, S., 2011, "Identification of Force Coefficients in Two Squeeze Film Dampers With a Central Groove," M.S. Thesis, Texas A&M University, College Station, TX.

[40] San Andrés, L., 2010, Monthly Progress Report #22 to Pratt & Whitney UTC,Technical Report No. 12, November 2010.

[41] San Andrés, L., 2010, "Monthly Progress Report #20 to Pratt & Whitney UTC," Technical Report No. 20, September 2010.

[42] Fritzen, C.-P., 1986, "Identification of Mass, Damping and Stiffness Matrices of Mechanical Systems," J. Vib. Acoust. Stress. Reliab. Des. , **108**, pp. 9-16.

[43] San Andrés, L., 2010, "Experimental Identification of Bearing Force Coefficients " Modern Hydrodynamic Lubrication Theory, Notes 14, Texas A&M University Digital Libraries,https://repository.tamu.edu/handle/1969.1/93197, 01/02/2011.

[44] San Andrés, L., 2009, Monthly Progress Report #12 to Pratt & Whitney UTC, Technical Report No. 12, November 2009.

[45] Vance, J. M., 1988, "*Rotordynamics of Turbomachinery*," John Wiley & Sons, New York.

[46] San Andrés, L., 2010, "Identification of Force Coefficients for Two Open Ends SFD Configurations: Long and Short Journals," Mid-Year Report 2010, July 2010.

APPENDIX A

SHORT LENGTH AND LONG DAMPER SFD FORCE COEFFICIENTS

This appendix presents the SFD force coefficients for the two sealed ends dampers derived from circular orbit tests described in Chapters VI and VII.

Table A.1 lists the direct and cross coupled SFD coefficients for the sealed ends long damper identified from circular orbits of amplitude $r = 0.054c_A$ at the centered condition (e_S=0) and two static eccentricities (e_S=0.18c_A and 0.36c_A) for whirl frequencies ranging from 110 to 250 Hz. Note that the direct and cross coupled SFD stiffness coefficients are negligible for eccentricities equal to 0 and 0.18c_A , but are significant for the highest eccentricity (e_S=0.36c_A).

Table A.2 lists the direct and cross coupled SFD force coefficients for the sealed ends short length damper, determined from circular orbits centered (e_S=0) and at two static eccentricities (e_S=0.18c_B and 0.37c_B). The frequency range of parameter identification is 50 – 250 Hz. Appendix B lists details the uncertainty of the identified parameters, and appendix C lists the goodness of fit of physical the model with the test data.

Table A.1 Sealed long SFD: direct and cross-coupled force coefficients derived from circular orbit tests. Frequency range 110 – 210 Hz, Sealed ends

Eccentricity (μm)	Static load (N)	whirl amplitude r (μm)	SFD Direct Coefficients					
			K_{XX} (MN/m)	K_{YY} (MN/m)	M_{XX} (kg)	M_{YY} (kg)	C_{XX} (kN-s/m)	C_{YY} (kN-s/m)
0	0	7.62	-0.6	0.4	65.4	68.1	54.3	60.4
25.4	110	7.62	-0.6	-0.1	60.3	62.1	53.8	56.2
50.8	220	7.62	6.2	5.6	71.0	70.3	61.1	63.4

Eccentricity (μm)	Static load (N)	whirl amplitude r (μm)	SFD Cross-Coupled Coefficients					
			K_{XY} (MN/m)	K_{YX} (MN/m)	M_{XY} (kg)	M_{YX} (kg)	C_{XY} (kN-s/m)	C_{YX} (kN-s/m)
0	0	7.62	2.9	1.4	7.0	5.8	9.8	8.3
25.4	110	7.62	-0.7	0.1	2.4	0.1	3.5	4.2
50.8	220	7.62	4.1	6.7	7.4	9.2	9.5	8.3

Table A.2 Sealed short length SFD: direct and cross-coupled force coefficients derived from circular orbit tests. Frequency range 50 – 250 Hz, Sealed ends

Eccentricity (μm)	Static load (N)	whirl amplitude r (μm)	SFD Direct Coefficients					
			K_{XX} (MN/m)	K_{YY} (MN/m)	M_{XX} (kg)	M_{YY} (kg)	C_{XX} (kN-s/m)	C_{YY} (kN-s/m)
0.0	0.0	7.62	-1.3	-0.7	17.7	20.1	12.8	13.8
25.4	480.4	7.62	-0.1	0.1	19.1	20.0	12.7	12.8
50.8	960.8	7.62	0.3	0.2	19.6	19.6	14.1	13.4

Eccentricity (μm)	Static load (N)	whirl amplitude r (μm)	SFD Cross-Coupled Coefficients					
			K_{XY} (MN/m)	K_{YX} (MN/m)	M_{XY} (kg)	M_{YX} (kg)	C_{XY} (kN-s/m)	C_{YX} (kN-s/m)
0.0	0.0	7.6	0.7	0.3	1.5	-0.1	1.2	0.2
25.4	480.4	7.6	0.9	0.9	1.8	0.6	1.2	0.7
50.8	960.8	7.6	0.9	1.7	0.9	1.4	2.6	1.9

APPENDIX B

UNCERTAINTY ANALYSIS

This appendix details the uncertainty in the measurements and estimated parameters conveyed in this thesis. Appendix C lists the goodness of fit of physical the model with the test data.

Static tests.

The groove pressure is recorded with a single digit precision (±0.05psi) thus the uncertainty of the groove pressure measurement (U_{PG})= ±3.4475x10^{-3}bar.

The static load is recorded with no decimals hence the uncertainty of the measurement (U_{SL}) is δ ±2.22 N (±0.5 lbf). The displacement is measured with a voltmeter with 3 digit precision U_{δ}=±0.254μm.

The general equation used to calculate the uncertainty of parameters that are estimated from direct relations (i.e. $r=f(x_1,x_2,..x_n)$) is defined as

$$U_r = \sqrt{\left(\frac{\partial r}{\partial z_1}U_{z_1}\right)^2 + \left(\frac{\partial r}{\partial z_2}U_{z_2}\right)^2 + ... + \left(\frac{\partial r}{\partial z_n}U_{z_n}\right)^2} \tag{B1}$$

where $U_{z_1}, U_{z_2}, ...U_{z_N}$ are the individual uncertainties for the input parameter set $\{z_i\}_{i=1,N}$. The expression for the uncertainty for the static stiffness is

$$\frac{U_{KS}}{K_S} = \sqrt{\left(\frac{U_F}{F}\right)^2 + \left(\frac{U_\delta}{\delta}\right)^2} \tag{B2}$$

Dynamic load tests

The DAQ board records the dynamic loads and displacements as voltage signals up to the fifth decimal place which determines the uncertainty of the recorded signals

rendering very low uncertainties U_F=4.48·10^{-3}N and U_δ=±1.27·10^{-4}μm. For the dynamic load the manufacturer specifies U_F /F=0.01 (1% linearity)

The DAQ acquires 4,096 samples at a rate of 16,384samples/second, hence the uncertainty of the frequency U_ω=4 Hz (25.2 rad/s). The identified coefficients are functions of the measured parameters (displacement, force, and frequency). The relations to estimate the linearized stiffness K, viscous damping C, and inertia M force coefficients are[7]

$$\begin{aligned} K &= \frac{\partial F}{\partial x} \rightarrow K \sim \frac{F}{\delta}; \\ C &= \frac{\partial F}{\partial \dot{x}} \rightarrow C \sim \frac{F}{i\delta\omega}; \\ M &= \frac{\partial F}{\partial \ddot{x}} \rightarrow M \sim \frac{F}{-\delta\omega^2} \end{aligned} \tag{B3}$$

From equation B2, the uncertainties for the estimated physical parameters are

$$\begin{aligned} \left(\frac{U_K}{K}\right) &= \sqrt{\left(\frac{U_\delta}{\delta}\right)^2 + \left(\frac{U_F}{F}\right)^2} \\ \left(\frac{U_C}{C}\right) &= \sqrt{\left(\frac{U_\delta}{\delta}\right)^2 + \left(\frac{U_F}{F}\right)^2 + \left(\frac{U_\omega}{\omega}\right)^2} \\ \left(\frac{U_M}{M}\right) &= \sqrt{\left(\frac{U_\delta}{\delta}\right)^2 + \left(\frac{U_F}{F}\right)^2 + \left(2\frac{U_\omega}{\omega}\right)^2} \end{aligned} \tag{B4}$$

Note that Eq. (B3) uses the amplitudes of dynamic load and BC displacement. For the damping and inertia force coefficients, the maximum frequency (ω) in the identification procedure is used, i.e. 250 Hz.

[7] The equations below are referential only. The identification procedure follows a rigorous physical analysis. Better say, below the force noted is that needed to determine the coefficient.

Table B.1 Uncertainty of estimated force coefficients for the short and long dampers

	Short length damper		Long damper	
Test Frequency	50 Hz	210 Hz	110 Hz	250 Hz
U_K/K	1.0%	1.0%	1.0%	1.0%
U_C/C	8.1%	2.2%	3.8%	2.1%
U_M/M	16.0%	3.9%	7.3%	3.8%

APPENDIX C

GOODNESS OF FIT FOR IDENTIFIED PARAMETERS

For the two sealed damper configurations, the following tables present the goodness of model curve fits (R^2) for the real and imaginary parts of the mechanical impedance functions

In general the physical model shows very good correlation factors (goodness of fit), with the experimental mechanical impedance, for both, the real and imaginary parts of the mechanical impedance. In most cases R^2>0.95 indicating that the test data agrees well with the assumed physical model Re(H)=K-$M\omega^2$ and Im(H)=$C\omega$. Appendix C lists the goodness of fit of physical the model with the test data.

Table C.1 Goodness of fit of real and imaginary parts of the mechanical impedance for lubricated test system, centered and at two static eccentricities. Circular orbits of amplitude r=0.055c_B. Frequency range 50 – 210 Hz, Sealed ends short length SFD

Eccentricity ratio (e_S/c_B)	Goodness of fit			
	Re (XX)	Re (YY)	Im (XX)	Im (YY)
0.00	0.997	0.994	0.988	0.980
0.18	0.989	0.976	0.964	0.921
0.37	0.978	0.974	0.917	0.802

Table C.2 Goodness of fit of real and imaginary parts of the mechanical impedance for lubricated test system, centered and at two static eccentricities. Circular orbits of amplitude r=0.055c_B. Frequency range 110 – 220 Hz, Sealed ends long SFD

Eccentricity ratio (e_S/c_A)	Goodness of fit			
	Re (XX)	Re (YY)	Im (XX)	Im (YY)
0.00	0.998	0.999	0.993	0.998
0.18	0.985	0.995	0.918	0.938
0.36	0.992	0.996	0.966	0.960

APPENDIX D

SFD FORCE COEFFICIENTS FROM CLASSICAL LUBRICATION THEORY AND NONDIMENSIONALIZATION OF SFD FORCE COEFFICIENTS [39]

Classical lubrication theory assumes the central groove as a flow source of uniform pressure, dividing the flow region into two separate squeeze film dampers working in parallel [10]. Predictive formulas for damping and added mass coefficients in a full film open ends centered damper are used to normalize the experimental force coefficients. For small amplitude motions ($r/c<<1$) these coefficients are: [10]

$$C^* = 2\cdot 12\pi\mu L\left(\frac{D}{2c}\right)^3\left[1-\frac{\tanh\left[L/D\right]}{L/D}\right] = C^*_{XX} = C^*_{YY}$$
$$M^* = 2\cdot\frac{\pi\rho L}{c}\left(\frac{D}{2}\right)^3\left[1-\frac{\tanh\left[L/D\right]}{L/D}\right] = M^*_{XX} = M^*_{YY} \qquad \text{(D1)}$$

The factor two in the equation above accounts for the two film lands adjacent to the groove. The parameters (μ, ρ) denote the lubricant viscosity and lubricant density and (D=2R, L, c) denote the journal diameter, land length and radial clearance, respectively. Table D.1 presents the normalizing damping and mass coefficients for the short length and long dampers. Note that the two damper configurations have different normalizing coefficients; hence, the normalized coefficients are not comparable from one configuration to the other (short and long). Table D.1 lists the normalizing coefficients (C^*, M^*)for the short length and long dampers.

Table D.1 Predicted normalizing force coefficients for the short and long dampers [39]

Long damper Land length L_A=2.54 cm, clearance c_A=141.0μm	C_A^* (kN-s/m)	M_A^* (kg)
	6.798	2.985
Short length damper Land length L_B=1.27 cm, clearance c_B=137.9μm	C_B^* (kN-s/m)	M_B^* (kg)
	0.918	0.386

VITA

Name:	Lady Paola Mahecha Mojica
Address:	Department of Mechanical Engineering, 3123 TAMU, College Station, TX 77843, USA
Email Address:	paolita_mahecha@hotmail.com
Education:	B.En., Mechanical Engineering, Universidad de los Andes at Bogotá, Colombia, 2009
	B.En., Electronic Engineering, Universidad de los Andes at Bogotá, Colombia, 2009
	M.S., Mechanical Engineering, Texas A&M University,2011